

Glueball Properties at Finite Temperature in SU(3) Anisotropic Lattice QCD

Noriyoshi Ishii

*The Institute of Physical and Chemical Research (RIKEN),
2-1 Hirosawa, Wako, Saitama 351-0198, Japan*

Hideo Suganuma

*Faculty of Science, Tokyo Institute of Technology,
2-12-1 Ohkayama, Meguro, Tokyo 152-8551, Japan*

Hideo Matsufuru

*Yukawa Institute for Theoretical Physics, Kyoto University,
Kitashirakawa-Oiwake, Sakyo, Kyoto 606-8502, Japan*

The thermal properties of the glueballs are studied using SU(3) anisotropic lattice QCD with $\beta_{\text{lat}} = 6.25$, the renormalized anisotropy $\xi \equiv a_s/a_t = 4$ over the lattice of the size $20^3 \times N_t$ with $N_t = 24, 26, 28, 30, 33, 34, 35, 36, 37, 38, 40, 43, 45, 50, 72$ at the quenched level. To construct a suitable operator for the lowest-state glueball on the lattice, we adopt the smearing method, providing an illustration of its physical meaning in terms of the operator size. First, we construct the temporal correlators $G(t)$ for the lowest 0^{++} and 2^{++} glueballs, using more than 5,000 gauge configurations at each temperature T . We then perform the pole-mass measurement of the thermal glueballs from $G(t)$. For the lowest 0^{++} glueball, we observe a significant pole-mass reduction of about 300 MeV in the vicinity of T_c or $m_G(T \simeq T_c) \simeq 0.8m_G(T \sim 0)$, while its size remains almost unchanged as $\rho(T) \simeq 0.4$ fm. Finally, for completeness, as an attempt to take into account the effect of thermal width $\Gamma(T)$ at finite temperature, we perform a more general new analysis of $G(t)$ based on its spectral representation. As an ansatz to the spectral function $\rho(\omega)$, we adopt the Breit-Wigner form, and perform the best-fit analysis of the temporal correlator as a straightforward extension to the standard pole-mass analysis. The result indicates a significant broadening of the peak as $\Gamma(T) \sim 300$ MeV as well as rather modest reduction of the peak center of about 100 MeV near T_c for the lowest 0^{++} glueball. The temporal correlators of the color-singlet modes corresponding to these glueballs above T_c are also investigated.

PACS numbers: 12.38.Gc, 12.39.Mk, 12.38.Mh, 11.15.Ha

I. INTRODUCTION

QCD at finite temperature is one of the most interesting subjects in the quark hadron physics [1, 2, 3]. At low temperature, quarks and gluons are confined in the color-singlet objects, hadrons, due to the nonperturbative effect of the strong interactions among them. With the increasing temperature, these interactions diminish due to the asymptotic freedom, which is expected to lead to liberation of quarks and gluons above a critical temperature T_c , forming the new phase, i.e., the quark-gluon plasma (QGP) phase.

At present, we are in front of the experimental possibility to create the QGP phase in the RHIC project at Brookhaven National Laboratory. Hence, much progress is desired in the theoretical understanding of QCD at finite temperature. To study QCD at finite temperature and to understand the QCD phase transition, the effective models and the lattice QCD Monte Carlo simulation provide useful and complementary approaches. While the effective models offer their own insights into the physical phenomena and often provide analytical methods to estimate related physical quantities, the lattice QCD simulation provides a model-independent method of calculating physical quantities directly based on QCD.

The SU(3) lattice QCD at the quenched level indicates the deconfinement phase transition of the weak first order at the critical temperature $T_c \simeq 260$ MeV [4], and simulations with dynamical quarks show the chiral phase transition at $T_c = 173(8)$ MeV for $N_f = 2$ and $T_c = 154(8)$ MeV for $N_f = 3$ in the chiral limit [5].

Above T_c , most of nonperturbative properties such as color confinement and spontaneous chiral-symmetry breaking disappear. Consequently, quarks and gluons are liberated, and the tremendous changes are expected in the mass spectrum.

Even below T_c , one is interested in the hadronic mass shift [2, 6, 7], because it can be one of the most important pre-critical phenomena of the QCD phase transition at finite temperature (and also at finite density). In this respect, from the experimental side for instance, CERES Collaboration [8] has proposed the high-energy heavy-ion collision data, which may indicate the mass shift of ρ -meson, and extensive theoretical efforts have been made aiming at understanding of its true implications [9].

The theoretical background to believe in the hadronic mass shift is as follows. As the temperature increases up close to T_c , the inter-quark potential is known to change significantly [10, 11]. As far as the heavy quarkonia are concerned, for instance J/ψ , the change of the inter-quark potential may be followed by the changes in the

structures of hadrons, which may lead to significant mass shifts as a consequence [2]. One also expects significant mass shifts of the light hadrons, for instance, σ -meson [6], which is due to the partial chiral restoration.

At finite temperature, due to the absence of the Lorentz invariance, the concept of the “mass” becomes less definitive, and there emerge two distinct concepts of the “screening mass” and the “pole mass”. The screening mass governs the correlations along the spatial direction, while the pole mass governs the correlations along the temporal direction. The relation between them is analogous to the relation between the Debye screening mass and the plasma frequency in electro dynamics [12]. Both of these two masses are interesting quantities, which can reflect the important non-perturbative features of QCD. However, we are interested here not in the screening mass but in the pole mass, because the pole mass is closely related to these experiments and calculations mentioned above. In fact, the pole mass is expected to be directly observed as the physical mass of the thermal hadrons.

In contrast to the effective model approaches, which have been extensively used to study the thermal properties of hadrons [2, 6], only a few lattice QCD studies have been performed for the pole mass of thermal hadrons so far [13, 14, 15, 16]. Instead, the screening mass has been extensively studied with the lattice QCD [12, 17, 18, 19] by analyzing the spatial correlations of the hadronic correlators. The reason behind this is the technical difficulty of measuring hadronic two-point correlators in the temporal direction at finite temperature on the lattice. In fact, since the temporal extension of the lattice shrinks as $1/T$ at high temperature, the pole-mass measurements have to be performed in the limited distance shorter than $1/(2T)$, which corresponds to $N_t/2 = 2-4$ near T_c in the ordinary isotropic lattice QCD [12].

The severe limitation on the measurement of the temporal correlation can be avoided with an anisotropic lattice where the temporal lattice spacing a_t is smaller than the spatial one a_s [20]. On the anisotropic lattice, by taking a small a_t , it is possible to use efficiently a large number of the temporal lattice points even in the vicinity of T_c , while the physical temporal extension $1/T = N_t a_t$ is kept fixed. In this way, the number of available temporal data are largely increased on the anisotropic lattice, and accurate pole-mass measurements from the temporal correlation become possible.

In this paper, we study the glueball properties at finite temperature from the temporal correlation in SU(3) anisotropic lattice QCD. The glueballs are special and interesting hadrons. They belong to a different class of hadrons. Unlike mesons and baryons, which mainly consist of valence quarks and anti-quarks, the glueballs mainly consist of gluons. Their existences are predicted in QCD as a consequence of the self-interactions among gluons. However, in the presence of the dynamical quarks, the glueballs are expected to mix with the mesons, which raises a difficulty in distinguishing them from ordinary mesons in experiments as well as in full lat-

tice QCD. To avoid this unsolved difficult problem, we adopt quenched lattice QCD as a necessary first step before attempting to include the effect of dynamical quarks in future. It is worth mentioning here that, even without dynamical quarks, quenched lattice QCD reproduces well various masses of hadrons, mesons and baryons, as well as the important nonperturbative quantities such as the string tension and the chiral condensate.

In quenched QCD, the elementary excitations are only glueballs in the confinement phase below the critical temperature $T_c \simeq 260$ MeV. From the lattice QCD studies at quenched level [21, 22, 23], the lightest physical excitation at zero temperature is known to be the scalar glueball with $J^{PC} = 0^{++}$ and the mass $m_G(0^{++}) \simeq 1500-1700$ MeV, and the next lightest one is the tensor glueball with $J^{PC} = 2^{++}$ and $m_G(2^{++}) \simeq 2000-2400$ MeV. These light glueballs are expected to play the important role in the thermodynamic properties of quenched QCD below T_c . Our aim is to understand the thermodynamic properties of quenched QCD below T_c from the view point of the thermal properties of the lowest-lying 0^{++} and the 2^{++} glueballs.

The contents are organized as follows. In Sect. II, we begin with a brief review of the spectral representation of the temporal glueball correlator. We then introduce the smearing method as a method to enhance the ground-state contribution in the glueball correlator, and consider the physical meaning of the smearing method as well as the prescription how to give a rough estimate of the glueball size based on the informations from the temporal glueball correlators with the smearing method. Sect. III is devoted to the brief descriptions of the lattice QCD action, its parameters and the critical temperature T_c in our anisotropic lattice. In Sect. IV, we construct the temporal glueball correlators based on SU(3) lattice QCD, and perform the pole-mass measurements assuming that the thermal width of the peak in the spectral function is sufficiently narrow. We study the low-lying 0^{++} and 2^{++} glueballs both below and above T_c . This procedure itself has been widely used in the standard mass measurements of various hadrons in the lattice QCD Monte Carlo calculations at zero temperature, and was also adopted by [13, 14] in the pole-mass measurements of various mesons at finite temperature. In Sect. V, we compare our results with the related lattice QCD results on the screening masses and the pole masses at finite temperature. In order to discuss the physical implications of our results, we establish a phenomenological relation among the critical temperature, the size and the pole-mass of the thermal glueballs based on an effective theory of the QCD phase transition, the closed packing model. The section is closed with the consideration what is the trigger of the QCD phase transition. In Sect. VI, for completeness, we perform a more general new analysis of the temporal correlators of glueballs as an attempt to take into account the effects of the possible appearance of the non-zero thermal width of the bound-state peak at finite temperature. We adopt Breit-Wigner ansatz for the form

of the spectral function to extract the center and the thermal width of the ground-state peak through the spectral representation. This procedure itself is a straightforward extension to the procedure adopted in the pole-mass measurements, which seems to be widely applicable to various temporal correlators of thermal hadrons. Sect. VII is devoted to the summary and concluding remarks.

II. THE SMEARING METHOD IN QUENCHED SU(3) LATTICE QCD

A. The spectral representation

Using the glueball operator $\phi_0(t, \vec{x})$, we consider the temporal correlator of the glueball as

$$G(t) \equiv \langle \phi(t) \phi(0) \rangle, \quad (1)$$

where $\phi(t)$ is the zero-momentum projected operator defined as

$$\begin{aligned} \phi(t) &\equiv \phi_0(t) - \langle \phi_0 \rangle, \\ \phi_0(t) &\equiv \frac{1}{N_s} \sum_{\vec{x}} \phi_0(t, \vec{x}), \end{aligned} \quad (2)$$

with $N_s = N_x N_y N_z$ being the number of sites in the spatial submanifold. The angular bracket $\langle \cdot \rangle$ denotes the statistical average. The subtraction of the vacuum expectation value is necessary for the 0^{++} glueball. The summation over \vec{x} is performed for the zero-momentum projection, i.e., the total momentum is set to be zero. The glueball operator $\phi_0(t, \vec{x})$ has to be properly constructed so as to have a definite spin and parity in the continuum limit. For instance, the 0^{++} and 2^{++} glueball operator are defined as [21, 22, 24, 25]

$$\begin{aligned} \phi_0(t, \vec{x}) &\equiv \text{ReTr} \left(P_{12}(t, \vec{x}) + P_{23}(t, \vec{x}) + P_{31}(t, \vec{x}) \right), \\ \phi_0(t, \vec{x}) &\equiv \text{ReTr} \left(2P_{12}(t, \vec{x}) - P_{23}(t, \vec{x}) - P_{31}(t, \vec{x}) \right), \end{aligned} \quad (3)$$

respectively, where $P_{ij}(t, \vec{x})$ denotes the plaquette operator in the i - j plane.

To consider the spectral representation, we express the temporal correlator $G(\tau)$ in the canonical operator representation as

$$G(\tau) = Z(\beta)^{-1} \text{tr} \left(e^{-\beta H} \phi(\tau) \phi(0) \right), \quad (4)$$

where $\beta = 1/T$ denotes the inverse temperature, $Z(\beta) \equiv \text{tr}(e^{-\beta H})$ the partition function, and H the Hamiltonian of QCD. The field operator $\phi(\tau)$ is represented in the imaginary-time Heisenberg picture as $\phi(\tau) = e^{\tau H} \phi(0) e^{-\tau H}$. By using the identity $G(\tau) = G(\beta - \tau)$ for the manifest periodicity, we obtain the spectral representation as

representation as

$$\begin{aligned} G(\tau) &= \frac{1}{2} \left(G(\tau) + G(\beta - \tau) \right) \\ &= \sum_{n,m} \frac{|\langle n | \phi | m \rangle|^2}{2Z(\beta)} \exp \left(-\beta \frac{E_m + E_n}{2} \right) \\ &\quad \times \cosh \left[(\tau - \beta/2)(E_n - E_m) \right] \\ &= \int_{-\infty}^{\infty} \frac{d\omega}{2\pi} \frac{\rho(\omega)}{2 \sinh(\beta\omega/2)} \cosh \left(\omega(\beta/2 - \tau) \right), \end{aligned} \quad (5)$$

where E_n denotes the energy of the n -th excited state $|n\rangle$. In this paper, $|0\rangle$ denotes the vacuum, and $|1\rangle$ denotes the lowest glueball state. Here, $\rho(\omega)$ denotes the spectral function defined as

$$\begin{aligned} \rho(\omega) &= \sum_{n,m} \frac{|\langle n | \phi | m \rangle|^2}{Z(\beta)} e^{-\beta E_m} \\ &\quad \times 2\pi \left(\delta(\omega - E_n + E_m) - \delta(\omega - E_m + E_n) \right), \end{aligned} \quad (6)$$

with the property

$$\begin{aligned} \rho(\omega) &\geq 0 \quad \text{for } \omega > 0, \\ \rho(\omega) &\leq 0 \quad \text{for } \omega < 0. \end{aligned} \quad (7)$$

Due to the bosonic nature of the glueballs, $\rho(\omega)$ is odd in ω .

The spectral function $\rho(\omega)$ is the residue of the glueball correlator in the Fourier representation as

$$G(\omega_l) = \int_0^\beta d\tau e^{-i\omega_l \tau} G(\tau) = \int_{-\infty}^{\infty} \frac{d\omega'}{2\pi} \frac{\rho(\omega')}{i\omega_l - \omega'}, \quad (8)$$

where $\omega_l \equiv \frac{2\pi l}{\beta}$ denotes the Matsubara frequency for bosons. It is also the residue of the retarded and advanced Green functions as

$$\begin{aligned} G_R(\omega) &= \int_{-\infty}^{\infty} \frac{d\omega'}{2\pi} \frac{\rho(\omega')}{\omega - \omega' + i\epsilon}, \\ G_A(\omega) &= \int_{-\infty}^{\infty} \frac{d\omega'}{2\pi} \frac{\rho(\omega')}{\omega - \omega' - i\epsilon}, \end{aligned} \quad (9)$$

respectively[26]. Hence, the information of the physical observables such as the mass and the width can be obtained by parameterizing the spectral function $\rho(\omega)$ properly and by performing the best-fit analysis to the lattice QCD Monte Carlo data of the temporal correlator $G(t)$ through the spectral representation Eq. (5).

B. The smearing method

For the study of the low-lying glueballs, it is important to extract the contributions of the low-lying states in lattice QCD Monte Carlo simulations. The smearing method is one of the most popular numerical techniques

to enhance the contributions from the low-lying states. Here, we give a brief review of the smearing method in SU(3) lattice QCD in the zero-temperature limit. In this limit $\beta \equiv 1/T \rightarrow \infty$, the spectral function $\rho(\omega)$ and the correlator $G(t)$ are simply expressed as

$$\rho(\omega) = \sum_n 2\pi A_n \left(\delta(\omega - E_n) - \delta(\omega + E_n) \right), \quad (10)$$

$$\frac{G(t)}{G(0)} = \sum_n C_n \exp(-E_n t),$$

with $A_n \equiv |\langle n | \phi | 0 \rangle|^2 / Z$ and

$$C_n \equiv \frac{A_n}{\sum_k A_k} = \frac{|\langle n | \phi | 0 \rangle|^2}{\sum_k |\langle k | \phi | 0 \rangle|^2}. \quad (11)$$

Note that C_n is a non-negative real number with $0 \leq C_n \leq 1$ with the normalization as $\sum C_n = 1$. It will be referred to as the overlap between the state $\phi|0\rangle$ and the n -th asymptotic state $|n\rangle$.

In general, to measure the ground-state mass from $G(t)$, one seeks for the region where contributions from excited states almost die out, leaving only the ground-state component as $G(t)/G(0) \simeq C_1 \exp(-E_1 t)$. In this region, one may perform the best-fit analysis with

$$C \exp(-m_G t) \quad (12)$$

to obtain the ground-state mass $m_G = E_1$ and the ground-state overlap $C = C_1$. (Here, as was mentioned in the previous subsection, $|1\rangle$ denotes the state of the lowest-lying glueball, while $|0\rangle$ denotes the vacuum state. Because $\phi(t)$ is the zero-momentum projected operator, defined in Eq. (2), E_n denotes the mass of the n -th state.) In principle, such a region always exists for enough large t in the zero-temperature case. However, in practice, it is difficult to use such large t in lattice QCD Monte Carlo calculations, since the correlator $G(t)$ decreases exponentially with t and becomes so small for the large t that it is comparable to its statistical error. Hence, to measure the mass of the ground-state, it is essential that the ground-state overlap C_1 should be sufficiently large. In the case of the glueballs in quenched SU(3) lattice QCD, the ground-state overlaps C_1 of the operators given in Eq. (3) are quite small, as long as they are constructed from the simple plaquette operators $P_{ij}(t, \vec{x})$. In this case, due to the considerable contributions from excited states, the measured mass with Eq. (12) always behaves as if it were much heavier. The difficulty of this small overlap originates from the fact that the plaquette operator has a smaller “size” of $O(a)$ than the physical size of the glueball [27]. This problem becomes severer near the continuum limit. Hence, for the accurate mass measurement, it is necessary to enhance the ground-state contribution by improving the glueball operator. This is achieved by making the operator have approximately the same size as the physical size of the glueball. The smearing method provides an iterative procedure to generate

such an extended operators, which is referred to as the smeared operators [21, 25, 27, 28].

The smeared operator is obtained by replacing the original spatial link variables $U_i(s)$ in the plaquette operators by the associated fat link variables $U_i^{(n)}(s)$. Starting from $U_i^{(0)}(s) \equiv U_i(s)$, the $(n+1)$ -th fat link variable $U_i^{(n+1)}(s) \in \text{SU}(3)$ is defined iteratively from $U_i^{(n)}(s)$ so as to maximize

$$\text{ReTr} \left(U_i^{(n+1)}(s) V_i^{(n)\dagger}(s) \right), \quad (13)$$

with

$$V_i^{(n)}(s) \equiv \alpha U_i^{(n)}(s) + \sum_{\pm, j \neq i} U_{\pm j}^{(n)}(s) U_i^{(n)}(s \pm \hat{j}) U_{\pm j}^{(n)\dagger}(s + \hat{i}), \quad (14)$$

where $U_{-\mu}^{(n)}(s) \equiv U_{\mu}^{(n)\dagger}(s - \hat{\mu})$. Here, $\alpha \in \mathbb{R}$ is referred to as the smearing parameter, which controls the speed of the smearing. The summation index j runs over only the spatial directions to avoid the artificial nonlocality in time. A schematic illustration of $V_i^{(n)}(s)$ is shown in Fig. 1. $U_i^{(n+1)}(s)$ is the closest SU(3) element to $V_i^{(n)}(s)$. It is easy to see that $V_i^{(n)}(s)$ and $U_i^{(n+1)}(s)$ hold the same gauge transformation properties with $U_i^{(n)}(s)$. Hence, the smearing method respects the gauge covariance. As the physically extended glueball operator, we adopt the n -th smeared operator, i.e., the plaquette operator which is constructed with the n -th fat link variables $U_i^{(n)}(s)$.

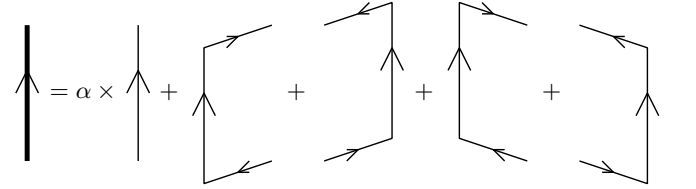


FIG. 1: The schematic illustration of $V_i^{(n)}(s)$. The thick line represents the variable $V_i^{(n)}(s)$. Thin lines represent the link variables $U_i^{(n)}(s)$.

C. The physical meaning of the smearing method

Here, we estimate the size of the n -th smeared operator and consider the physical meaning of the smearing method. To obtain the direct correspondence with the continuum theory, we adopt the lattice Coulomb gauge, which is defined so as to maximize

$$R \equiv \sum_s \sum_{k=1}^3 \text{ReTr} U_k(s), \quad (15)$$

with respect to SU(3) gauge transformations. In the continuum limit, we recover the continuum Coulomb gauge condition as

$$\partial_k A_k(x) = 0. \quad (16)$$

In this gauge, the spatial link-variable $U_k(s)$ becomes maximally continuous around 1, and can be safely expanded in a as $U_k(s) \equiv e^{iaA_k(s)} = 1 + iaA_k(s) + O(a^2)$ near the continuum limit. We consider the smearing with

the smearing parameter α . For convenience, we define

$$p \equiv \frac{\alpha}{\alpha + 4}, \quad q \equiv \frac{1}{\alpha + 4}, \quad (17)$$

which satisfy $p + 4q = 1$. As shown in Fig. 1, the $(n+1)$ -th smeared spatial gluon field $A_k(s; n+1)$ is iteratively described with the n -th smeared gluon field $A_k(s; n)$ as

$$\begin{aligned} A_x(s; n+1) &= pA_x(s; n) + q \left(A_y(s; n) + A_x(s + \hat{y}; n) - A_y(s + \hat{x} + \hat{y}; n) - A_y(s - \hat{y}; n) + A_x(s + \hat{y}; n) + A_y(s + \hat{x} - \hat{y}; n) \right. \\ &\quad \left. + A_z(s; n) + A_x(s + \hat{z}; n) - A_z(s + \hat{x} + \hat{z}; n) - A_z(s - \hat{z}; n) + A_x(s + \hat{z}; n) + A_z(s + \hat{x} - \hat{z}; n) \right) \end{aligned} \quad (18)$$

in the leading order in a . The expressions for $A_y(s; n+1)$ and $A_z(s; n+1)$ are similar. After some rearrangements, we obtain in the leading order in a

$$\begin{aligned} \partial_n A_x(s; n) &\equiv A_x(s; n+1) - A_x(s; n) \\ &= q \left\{ \partial_y A_x(s; n) - \partial_y A_x(s - \hat{y}; n) \right. \\ &\quad \left. + \partial_z A_x(s; n) - \partial_z A_x(s - \hat{z}; n) \right. \\ &\quad \left. - \partial_x A_y(s; n) + \partial_x A_y(s - \hat{y}; n) \right. \\ &\quad \left. - \partial_x A_z(s; n) + \partial_x A_z(s - \hat{z}; n) \right\} \\ &= q \left\{ (\partial_x^B \partial_x + \partial_y^B \partial_y + \partial_z^B \partial_z) A_x(s; n) \right. \\ &\quad \left. - \partial_x \partial_k^B A_k(s; n) \right\}. \end{aligned} \quad (19)$$

Here, ∂_k and ∂_k^B denote the forward and backward difference operators along k -axis ($k = x, y, z$), respectively, which are defined as

$$\begin{aligned} \partial_k f(s) &\equiv f(s + \hat{k}) - f(s), \\ \partial_k^B f(s) &\equiv f(s) - f(s - \hat{k}), \end{aligned} \quad (20)$$

respectively. Here, \hat{k} denotes the unit vector along the k -axis. By applying the continuum approximation both with respect to s and n , the difference operators ∂_n , ∂_k and ∂_k^B are then replaced by the derivatives $a_n \partial / \partial \tilde{n}$, $a_s \partial / \partial x_k$ and $a_s \partial / \partial x_k$, respectively. Here, $\tilde{n} \equiv na_n$ is the continuum parameter corresponding to n , and $a_n \in \mathbb{R}$ is formally introduced as a small constant interval in the n -direction, although the final result does not depend on a_n at all. In the continuum Coulomb gauge using Eq. (16), Eq. (19) reduces to the diffusion equation

$$a_n \frac{\partial}{\partial \tilde{n}} A_i(\vec{x}; n) = D \Delta A_i(\vec{x}; n) \quad \text{for } i = x, y, z, \quad (21)$$

where $D \equiv \frac{a_s^2}{\alpha + 4}$ works as the diffusion parameter. By solving this equation, the n -th smeared gauge field $A_i(\vec{x}; n)$ can be expressed by a linear combination of the original gluon field $A_i(\vec{x})$ as

$$\begin{aligned} A_i(\vec{x}; n) &= \int d^3y K(\vec{x} - \vec{y}; n) A_i(\vec{y}) \\ K(\vec{x}; n) &\equiv \frac{1}{\pi^{3/2} \rho^3} \exp\left(-\frac{\vec{x}^2}{\rho^2}\right), \end{aligned} \quad (22)$$

where the Gaussian extension ρ is defined as

$$\rho \equiv 2\sqrt{Dn} = 2a_s \sqrt{\frac{n}{\alpha + 4}}. \quad (23)$$

In this way, the n -th smeared gluon field physically corresponds to the Gaussian-distributed operator of the original gluon field. After the linearization of the gluon field, the n -th smeared plaquette is also expressed as the Gaussian-distributed operator. Here, the Gaussian extension ρ can be regarded as a characteristic size of the n -th smeared operator.

The expression of ρ in Eq. (23) explains the physical roles of the two parameters, α and n . The smearing parameter α plays the role of controlling the speed of the smearing, while, for each fixed α , n plays the role of extending the size of the smeared operator. Note that, for the larger α , the speed of smearing is the slower.

The smearing method was originally introduced to carry out the accurate mass measurement by maximizing the ground-state overlap [27]. However, we will use it to give a rough estimate of the physical glueball size. In fact, once we find the pair of the smearing parameters n and α , which achieves the maximum ground-state overlap, the physical size of the glueball is roughly estimated with Eq. (23).

With Eq. (22), we try to express the n -th smeared 0^{++} glueball operator in terms of the original gluon field

$A_\mu^a(x)$. Near the continuum limit, the zero-momentum projected 0^{++} glueball operator $\Phi_{\text{GB}}(0^{++}; n)$ consisting of the smeared link-variable $U_i^{(n)}(s)$ is expressed as

$$\Phi_{\text{GB}}(0^{++}; n) = \frac{1}{V} \int d^3x G_{ij}^a(\vec{x}, t; n) G_{ij}^a(\vec{x}, t; n), \quad (24)$$

where $G_{ij}^a(\vec{x}, t; n)$ is the field strength associated with the smeared gluon field $A_i^a(\vec{x}, t; n)$. Here, t can be regarded as a fixed parameter in this argument, and will be omitted hereafter. By inserting Eq. (22), $\Phi_{\text{GB}}(0^{++})$ is expressed with the original gauge field $A_i^a(\vec{x})$ as

$$\begin{aligned} \Phi_{\text{GB}}(0^{++}; n) &= \frac{1}{V} \int d^3x \int d^3y d^3z \left(\frac{\partial}{\partial x_i} K(\vec{x} - \vec{y}; n) A_j(\vec{y}) - \frac{\partial}{\partial x_j} K(\vec{x} - \vec{y}; n) A_i(\vec{y}) \right) \\ &\quad \times \left(\frac{\partial}{\partial x_i} K(\vec{x} - \vec{z}; n) A_j(\vec{z}) - \frac{\partial}{\partial x_j} K(\vec{x} - \vec{z}; n) A_i(\vec{z}) \right) + \dots \\ &= \frac{2}{V} \int \frac{d^3y d^3z}{\pi^{3/2} \rho^3} \exp\left(-\frac{(\vec{y} - \vec{z})^2}{2\rho^2}\right) \frac{\partial}{\partial y_j} A_i(\vec{y}) \frac{\partial}{\partial z_j} A_i(\vec{z}) + \dots \\ &= \frac{2}{V} \int \frac{d^3y d^3z}{\pi^{3/2} \rho^5} \left(3 - \frac{(\vec{y} - \vec{z})^2}{\rho^2} \right) \exp\left(-\frac{(\vec{y} - \vec{z})^2}{2\rho^2}\right) A_i(\vec{y}) A_i(\vec{z}) + \dots \end{aligned} \quad (25)$$

Here, “...” represents the terms which are more than quadratic in the gluon field, and are dropped off. In this derivation, partial integrations and the Coulomb gauge condition have been used. We expect that $\Phi_{\text{GB}}(0^{++}, n)$ is associated with the best pair of the smearing parameters n and α and works as an approximate “creation” operator of the 0^{++} glueball, which creates an approximate single glueball state from the vacuum.

D. The relation to Bethe-Salpeter amplitude

In the previous subsection, we proposed one possible method to give a rough estimate of the glueball size. In this subsection, we consider the relation between our estimate of the glueball size and the other estimate from the Bethe-Salpeter (BS) amplitude, which was adopted in Refs.[30, 31].

The size of the glueball is actually a nontrivial quantity. Although the charge radius of the glueball can be formally defined, its electric charges are carried by the quarks and anti-quarks, which play only of secondary roles in describing the glueball state in the idealized limit, since the glueball by its nature does not contain any va-

lence contents of (anti-)quarks.

In order to investigate the size of the glueball, the BS amplitude provides a convenient tool. The BS amplitude $\Psi(\vec{x}, \vec{y})$ is expressed as

$$\Psi_{\text{BS}}(\vec{y}, \vec{z}) \equiv \langle 0 | A_i(\vec{y}) A_i(\vec{z}) | G(\vec{P} = \vec{0}) \rangle, \quad (26)$$

which can be obtained as a solution of the BS equation. In the non-relativistic limit, it is expected to reduce to the glueball wave function in the first-quantized picture. This property has been exploited to estimate the size of the glueball in Ref.[30], where the size R_{BS} is introduced from the exponential decay of the tail of the BS amplitude as

$$\Psi_{\text{BS}}(\vec{r}, \vec{0}) \sim \exp(-|\vec{r}|/R_{\text{BS}}). \quad (27)$$

The connection between these two estimates is provided with Eq. (25) in the following way. We consider $\Phi_{\text{GB}}(0^{++}; n)$ associated with the best smearing with the Gaussian extension ρ . Since the ground-state overlap is maximized, the 0^{++} -glueball state can be approximated as

$$\begin{aligned} |G(\vec{P} = \vec{0})\rangle &\simeq \Phi_{\text{GB}}(0^{++}; n) |0\rangle \\ &= \frac{2}{V} \int \frac{d^3y d^3z}{\pi^{3/2} \rho^5} \left(3 - \frac{(\vec{y} - \vec{z})^2}{\rho^2} \right) \exp\left(-\frac{(\vec{y} - \vec{z})^2}{2\rho^2}\right) |A_i(\vec{y}) A_i(\vec{z})\rangle + \dots \\ &= \frac{2}{\pi^{3/2} \rho^5} \int d^3r \left(3 - \frac{\vec{r}^2}{\rho^2} \right) \exp\left(-\frac{\vec{r}^2}{2\rho^2}\right) |A_i(\vec{r}) A_i(\vec{0})\rangle + \dots, \end{aligned} \quad (28)$$

where we exploit the translational invariance and par-

tial integrations. Similar to Eq. (25), the states in

Eq. (28) such as $|G(\vec{P} = \vec{0})\rangle$ and $|A_i(\vec{y})A_i(\vec{z})\rangle$ are obtained through the gauge configuration generated in lattice QCD. Hence, this relation would provide a kind of nonperturbative construction of the glueball state in terms of the gluon field.

In the constituent gluon picture [32], the BS amplitude associated with Eq. (28) reduces to the following expression in the heavy effective gluon mass limit as

$$\begin{aligned}\Psi_{\text{BS}}(\vec{r}, \vec{0}) &\equiv \langle 0 | A_i(\vec{r}) A_i(\vec{0}) | G(\vec{P} = 0) \rangle \\ &\sim \frac{2}{\pi^{3/2} \rho^5} \left(3 - \frac{\vec{r}^2}{\rho^2} \right) \exp \left(-\frac{\vec{r}^2}{2\rho^2} \right).\end{aligned}\quad (29)$$

By comparing this with Eq. (27), we see that the size R_{BS} estimated with the BS amplitude is of the same magnitude as the characteristic size ρ of the smeared operator.

III. ANISOTROPIC LATTICE QCD

A. Lattice Parameter Set

We use the SU(3) plaquette action on an anisotropic lattice

$$\begin{aligned}S_G &= \frac{\beta_{\text{lat}}}{N_c} \frac{1}{\gamma_G} \sum_{s,i < j \leq 3} \text{ReTr} \left(1 - P_{ij}(s) \right) \\ &\quad + \frac{\beta_{\text{lat}}}{N_c} \gamma_G \sum_{s,i \leq 3} \text{ReTr} \left(1 - P_{i4}(s) \right),\end{aligned}\quad (30)$$

where $P_{\mu\nu}(s) \in \text{SU}(3)$ denotes the plaquette operator in the μ - ν -plane. The lattice parameter and the bare anisotropy parameter are fixed as $\beta_{\text{lat}} \equiv 2N_c/g^2 = 6.25$ and $\gamma_G = 3.2552$, respectively, so as to reproduce the renormalized anisotropy $\xi \equiv a_s/a_t = 4$ [20]. These parameters reproduce the spatial and the temporal lattice spacing as

$$\begin{aligned}a_s^{-1} &= 2.341(16) \text{ GeV}, \quad a_s \simeq 0.084 \text{ fm}, \\ a_t^{-1} &= 9.365(66) \text{ GeV}, \quad a_t \simeq 0.021 \text{ fm},\end{aligned}\quad (31)$$

respectively. Here, the scale unit is determined so as to reproduce the string tension as $\sqrt{\sigma} = 440$ MeV from the on-axis data of the static inter-quark potential. We perform the Monte Carlo calculations using the pseudo-heat-bath algorithm for the update of the gauge field configurations. The numerical calculations are performed on the lattice of the sizes $20^3 \times N_t$ with various N_t as $N_t = 24, 26, 28, 30, 33, 34, 35, 36, 37, 38, 40, 43, 45, 50, 72$, which correspond to the various temperatures listed in Table II. We note that the spatial lattice size of 20 corresponds to 1.68 fm in the physical unit. For all temperatures, we pick up gauge field configurations every 100 sweeps for measurements, after skipping more than 20,000 sweeps for the thermalization. The numbers N_{conf} of gauge configurations used in our calculations are summarized in Table II. Unless otherwise indicated, we divide the data into bins of the size 100 to reduce the

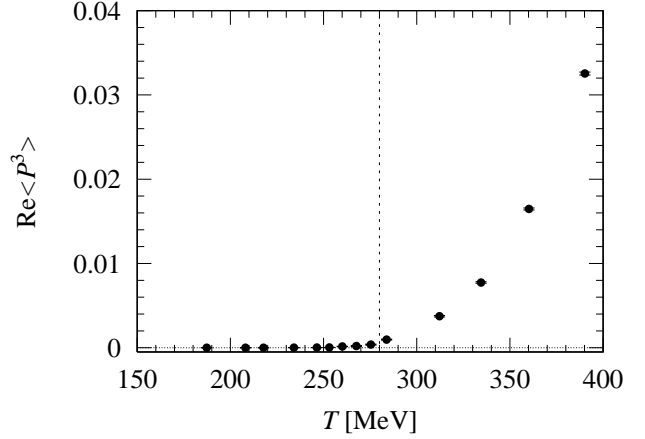


FIG. 2: The cubed Polyakov loop $\text{Re}\langle P^3 \rangle$ plotted against temperature. The vertical dotted line denotes the estimated critical temperature, $T_c \simeq 280$ MeV. The error bars are hidden inside the symbols.

possibly strong auto-correlations. However, the auto-correlations are not observed so strong in this simulation with the 100 sweep separation, since the separation by 100 sweeps seems already rather large.

The statistical errors are estimated with the jackknife analysis by regarding each bin as an independent data point.

As for the smearing parameters, which play the important role in extracting the ground-state contribution, we have checked that one of the best sets is provided as

$$\alpha = 2.1, \quad N_{\text{smr}} = 40, \quad (32)$$

in the present lattice calculation for the lowest 0^{++} and 2^{++} glueballs. We adopt this parameter set as the suitable smearing parameters for most of the calculations in this paper. As we shall see later, the temporal correlator $G(t)/G(0)$ and the pole mass m_G are almost insensitive to a particular choice of the smearing number N_{smr} , as far as $N_{\text{smr}} \sim 40$ with $\alpha = 2.1$. In fact, in a rather wide range as $30 \lesssim N_{\text{smr}} \lesssim 50$, $G(t)/G(0)$ and m_G are almost unchanged, and the ground-state overlap C is kept almost maximized. (See Fig. 6.) Only for the accurate measurement, we seek for the best value of N_{smr} with $\alpha = 2.1$ fixed, although the results are almost the same as those with $N_{\text{smr}} = 40$.

B. The critical temperature

Here, for completeness, we give an estimate of the critical temperature T_c on our anisotropic lattice, although the value of $T_c \simeq 260$ MeV with $\sqrt{\sigma} \simeq 420$ MeV is rather established on the isotropic lattice [4].

To estimate the critical temperature T_c , we consider

TABLE I: The lattice parameter $\beta = 2N_c/g^2$, the renormalized anisotropy $\xi = a_s/a_t$, the spatial lattice spacing a_s , the temporal lattice spacing a_t , the lattice size, the number of gauge field configurations skipped for thermalizations, the measurement interval of the gauge field configurations, the size of the bin, the suitable smearing parameters α and N_{smr} are summarized.

| β | $\xi = a_s/a_t$ | $a_s^{-1}[\text{GeV}]$ | $a_t^{-1}[\text{GeV}]$ | lattice size | thermalization | measurement interval | bin-size | smearing parameters |
|---------|-----------------|------------------------|------------------------|-------------------|----------------|----------------------|----------|-------------------------------------|
| 6.25 | 4 | 2.341(16) | 9.365(66) | $N_t \times 20^3$ | 20,000 | 100 | 100 | $\alpha = 2.1, N_{\text{smr}} = 40$ |

the Polyakov loop, which is defined as

$$\begin{aligned}
 P &\equiv \frac{1}{V} \int d^3x P(\vec{x}) \\
 &= \frac{1}{V} \int d^3x \text{Tr} \left(T \exp i \int_0^\beta dt A_0(\vec{x}, t) \right) \\
 &= \frac{1}{V} \int d^3x \text{Tr} \left(U_4(\vec{x}, 0) \cdots U_4(\vec{x}, N_t - 1) \right),
 \end{aligned} \tag{33}$$

where V denotes the volume of the space and T the time-ordering operation. As is well-known, its thermal expectation value $\langle P \rangle = \frac{1}{N_{\text{conf}}} \sum_{k=1}^{N_{\text{conf}}} P_k$, averaged over lots of gauge configurations, is an order parameter of quark confinement associated with the center \mathbb{Z}_3 symmetry [24, 25], where P_k denotes the value of the Polyakov loop P with the k -th configuration. However, to be strict, it is only in the thermodynamic limit with the infinite volume that Eq. (33) can work as the order parameter to estimate T_c . Note that, since the size of the lattice is limited, tunnelings from one vacuum to another are unavoidable for large simulation time even in the \mathbb{Z}_3 broken phase. As a consequence, due to the associated cancellation of the center \mathbb{Z}_3 -phase factor, $\langle P \rangle$ finally vanishes on the finite lattice, which raises a technical difficulty in estimating T_c from $\langle P \rangle$. To avoid this, instead of using the total expectation value itself, one often analyzes the scattering plot, a plot of P_k for each configuration labeled by k .

Here, for convenience, we analyze the thermal expectation value of the cubed Polyakov loop as

$$\langle P^3 \rangle = \frac{1}{N_{\text{conf}}} \sum_{k=1}^{N_{\text{conf}}} (P_k)^3, \tag{34}$$

which provides the equivalent result for the estimate of the critical temperature T_c with the scattering plot. We note that $\langle P^3 \rangle$ is not the order parameter of the confinement phase in a strict sense, since it is invariant under the center \mathbb{Z}_3 transformation. In general, in the symmetric phase, the expectation value of the order parameter vanishes due to the cancellation of the phase factor associated with the symmetry transformations, which never happens in the broken symmetry phase. However, in the specific case of $\langle P \rangle$, it is known from the analysis of the scattering plot that the norm of P_k for each configuration is already quite small in the symmetric phase, due to which its expectation value $\langle P \rangle$ almost vanishes even without involving the cancellation of the center \mathbb{Z}_3

phase factor. In contrast, P_k takes a manifestly non-vanishing value for each configuration in the broken symmetry phase, which can be used to identify the critical temperature T_c .

Such a tendency is quantitatively described with the cubed Polyakov loop $\langle P^3 \rangle$. In fact, in the plot of $\langle P^3 \rangle$ versus temperature T , the critical temperature T_c is characterized as the point where it begins to have a non-vanishing value.

In Fig. 2, $\langle P^3 \rangle$ is plotted against temperature. By taking into account the finite size effects which smoothen the phase transition, we estimate the critical temperature as $T_c \simeq 260\text{--}280$ MeV, which is consistent with the previous studies in Ref. [4], i.e., $T_c/\sqrt{\sigma} = 0.629(3)$.

For more accurate determination of the critical temperature T_c , we investigate the Polyakov-loop susceptibility χ , which is defined as [29]

$$\begin{aligned}
 \chi &\equiv \langle \Omega^2 \rangle - \langle \Omega \rangle^2 \\
 \Omega &\equiv \begin{cases} \text{Re} P \exp \left(-i \frac{2\pi}{3} \right), & \arg P \in [\pi/3, \pi), \\ \text{Re} P, & \arg P \in [-\pi/3, \pi/3), \\ \text{Re} P \exp \left(i \frac{2\pi}{3} \right), & \arg P \in [-\pi, -\pi/3). \end{cases}
 \end{aligned} \tag{35}$$

In Fig. 3, the Polyakov loop susceptibility is plotted against temperature. To obtain χ , about 1000 gauge configurations are used at each temperature near T_c , which are divided into bins of the size 50. The statistical errors are estimated with the jackknife analysis. In Fig. 3, we observe that a sharp peak is located between $T = 275$ MeV and $T = 284$ MeV. Hence, we identify the critical temperature of our lattice as $T_c \simeq 280$ MeV.

IV. NUMERICAL RESULTS —TEMPORAL CORRELATIONS AND POLE MASSES

In this section, we construct the temporal glueball correlator $G(t)$ at finite temperature, and perform the pole mass measurement. We adopt the procedure used in [13] as the standard one to extract the pole mass $m_G(T)$ of the thermal glueball from the temporal correlator $G(t)$ at temperature T by using the best-fit analysis with the fit function of single-cosh type considered later. Here, we regard each glueball as a quasi-particle and assume that the thermal width Γ of the ground-state peak is enough narrow in the spectral function $\rho(\omega)$. From the viewpoint of the spectral representation Eq. (5), such a narrowness

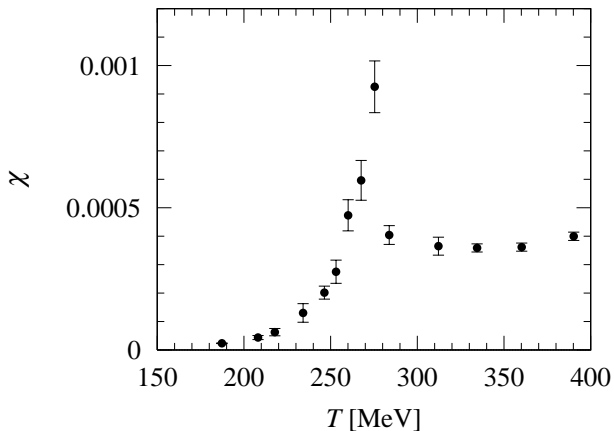


FIG. 3: The susceptibility χ of the Polyakov-loop plotted against the temperature. There is a sharp peak around $T = 280$ MeV, which indicates the critical temperature T_c of the phase transition in quenched $SU(3)_c$ QCD.

of the peak is necessary to identify the pole mass as a definite object and also to justify this standard procedure in a strict sense. (In Sect. VI, we will analyze our lattice QCD data without assuming the narrowness of the peak as a straightforward extension to the current analysis.)

Suppose that the thermal width is sufficiently narrow, i.e., $\Gamma \simeq 0$. Then, the spectral function $\rho(\omega)$ receives the contribution from the ground-state in the following manner:

$$\rho(\omega) = 2\pi A \left(\delta(\omega - m_G) - \delta(\omega + m_G) \right) + \dots, \quad (36)$$

where “...” represents the contributions from excited-states, and $A \equiv A(T)$ and $m_G \equiv m_G(T)$ are the strength and the pole-mass of the glueball peak at temperature T , respectively. Note that the appearance of the second delta function is due to the fact that the spectral function $\rho(\omega)$ is odd in ω , which reflects the bosonic nature of the glueball. Corresponding to Eq. (36), by inserting it into the spectral representation Eq. (5), the ground state contribution to the temporal correlator $G(t)$ is expressed as

$$G(t) = \frac{A}{1 - e^{-\beta m_G}} \left(e^{-tm_G} + e^{-(\beta-t)m_G} \right) + \dots. \quad (37)$$

Hence, after the ground state contribution is sufficiently enhanced, the appropriate fit function for $G(t)/G(0)$ is the following single hyperbolic cosine as

$$g(t) \equiv C \left(e^{-tm_G} + e^{-(\beta-t)m_G} \right), \quad (38)$$

where C and m_G are understood as the fit parameters. We will refer to C as the ground-state overlap, and to the fit function of $g(t)$ as the fit function of single-cosh type for simplicity.

For the accurate measurement, it is required that $G(t)$ is dominated by the ground-state contribution in the fit-range. (We consider the determination of the fit range

in the next subsection with an explicit example.) In this case, $g(t)$ can properly represent the ground-state contribution in Eq. (37), and C and m_G can be extracted accurately. In the actual calculations, the complete elimination of all the remaining contributions of the excited states is impossible. Since each hyperbolic cosine component contributes to $G(t)$ positively as is seen in the spectral representation Eq. (5), we always have the following inequalities as

$$g(0) \leq 1, \text{ and } C = \frac{g(0)}{1 + e^{-\beta m_G}} \leq \frac{1}{1 + e^{-\beta m_G}}. \quad (39)$$

Here, $g(0)$ and C take their maxima, if and only if $G(t)$ is completely dominated by the ground-state contribution in the whole region $0 \leq t \leq \beta$. In this case, we have the following equalities instead:

$$g(0) = 1, \text{ and } C = \frac{1}{1 + e^{-\beta m_G}}. \quad (40)$$

We thus see that $g(0) \simeq 1$ and $C \simeq 1/(1 + e^{-\beta m_G}) \simeq 1$ can both work as a criterion to determine whether the ground-state enhancement is sufficient or not. We will refer to $g(0)$ as the normalized ground-state overlap. Note that C differs from $g(0)$ only through the factor $1/(1 + e^{-\beta m_G})$, which is independent of both the smearing parameters α and N_{smr} . In this section, we examine C to determine if the ground-state enhancement is sufficient or not. We prefer C rather than $g(0)$ because of the following reasons. (i) The ground-state overlap C is directly obtained from the best-fit analysis with Eq. (38) as one of the best-fit parameters. (ii) In our previous work [16], C has been used for the criterion. However, $g(0) \simeq 1$ has the advantage over $C \simeq 1$ in Sect. VI, where the counterpart of C cannot be properly defined, whereas the counterpart of $g(0)$ can. At any rate, as is seen in Tables II and III, they are not so different from each other in numerical value, especially below T_c .

A. Thermal 0^{++} glueball

In Fig. 4 (a), we show the 0^{++} glueball correlator for the low temperature case $T = 130$ MeV after the suitable smearing as Eq. (32). We perform the best-fit analysis of the single-cosh type Eq. (38) with the two fit parameters, the ground-state overlap C and the pole-mass m_G of the lowest thermal glueball. The solid line denotes the result of this best-fit analysis. The fit-range is indicated by the vertical dotted lines.

1. The fit range

We consider the determination of the fit-range. Even after the ground-state enhancement is performed, the complete elimination of all the contributions of the excited states is impossible, especially in the neighborhood

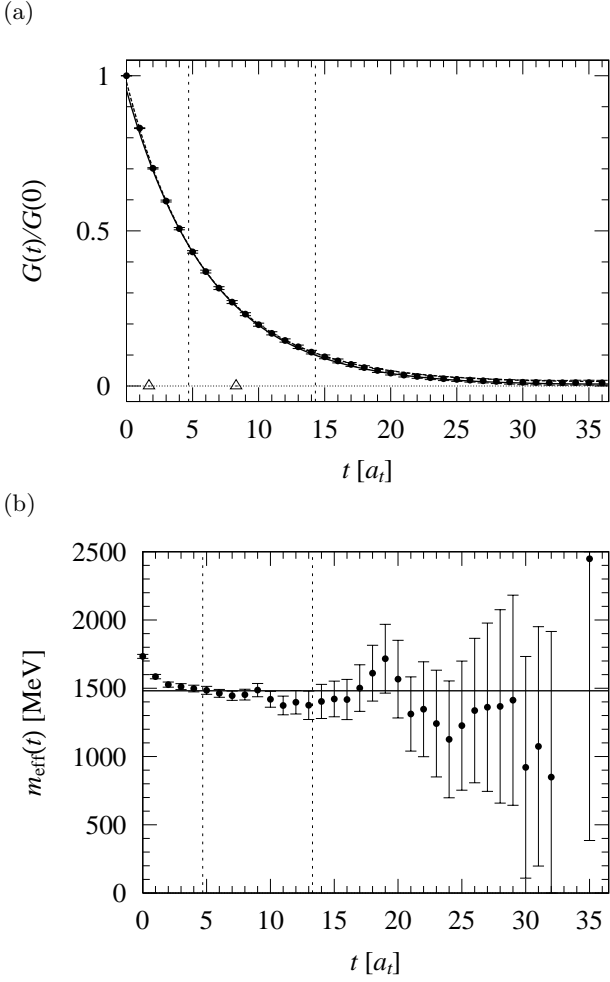


FIG. 4: (a) The temporal correlator $G(t)/G(0)$ of the 0^{++} glueball at the low temperature ($T = 130$ MeV) after the suitable smearing as Eq. (32). (b) The corresponding cosh-type effective-mass plot. In both figures, the solid lines represent the best single hyperbolic-cosine fitting in the plateau, which is indicated by the vertical dotted lines. The errorbars are estimated with the jackknife analysis. The dashed curve in (a) denotes the result of the best-fit analysis of Breit-Wigner type performed in the interval indicated by the two open triangles. (See Sect. VI and Eq. (55) for detail.)

of $t \sim 0 \pmod{\beta}$. It follows that the equality Eq. (37) holds only in a limited interval, which does not include the neighborhood of $t \sim 0$. Hence, for the accurate measurement of the pole-mass m_G , we need to find the appropriate fit-range, where contributions from excited states almost die out. To this end, we examine the effective-mass plot. The effective mass $m_{\text{eff}}(t)$ is defined as the solution to the following equation as

$$G(t+1)/G(t) = \frac{\cosh\left((t+1 - N_t/2)a_t m_{\text{eff}}(t)\right)}{\cosh\left((t - N_t/2)a_t m_{\text{eff}}(t)\right)}, \quad (41)$$

for a given $G(t+1)/G(t)$ at each fixed t . In Fig. 4 (b), we plot the effective mass $m_{\text{eff}}(t)$ against t associated

with Fig. 4 (a). We see that there appears a plateau, a region where $m_{\text{eff}}(t)$ takes almost a constant value. In this region, it is expected that $G(t)$ consists of nearly a single spectral component, and, hence, $g(t)$ can properly represent the ground-state contribution in Eq. (37). Note that, if more than a single state contribute with their different masses, a nontrivial t -dependence will appear in $m_{\text{eff}}(t)$. In the zero-temperature case, the plateau in the effective-mass plot is widely used as a candidate for the fit range in the best-fit analysis of single-cosh type Eq. (38). Here, the role of the smearing method is to suppress the excited-state contributions as much as possible, so that the plateau can be obtained with the smallest possible t .

In Fig. 4, the plateau is indicated by the vertical dotted lines, which is used to determine the fit-range. In this low temperature case $T = 130$ MeV, the best-fit analysis shows $C = 0.953(7)$ and $m_G = 1482(25)$ MeV, which seems consistent with $m_G \simeq 1500\text{--}1700$ MeV at $T \simeq 0$ MeV. We note that the ground-state overlap $C = 0.95$ becomes enough large owing to the suitable smearing.

In Fig. 5 (a), we show the 0^{++} glueball correlator for the high temperature case $T = 253$ MeV ($< T_c$) after the suitable smearing as Eq. (32). The solid line denotes the result of the best-fit analysis of the single-cosh type. The fit-range is indicated by the vertical dotted lines, which is determined from the plateau in the corresponding effective-mass plot Fig. 5 (b). We obtain $C = 0.89(1)$ and $m_G = 1289(26)$ MeV. Owing to the suitable smearing, contributions from the excited state are seen suppressed ($C \simeq 1$).

2. The ground-state overlap

In Fig. 6, the ground-state overlap C and the pole mass m_G for the 0^{++} glueball are plotted against the smearing number N_{smr} for the two cases (i) the low temperature case $T = 130$ MeV (circle), (ii) the high temperature case $T = 253$ MeV (triangle) below T_c . Here, we fix one of the smearing parameters as $\alpha = 2.1$. We see that, in the region $N_{\text{smr}} < 30$, with increasing N_{smr} , the ground state overlap C is growing and the pole-mass m_G is reducing. Then, in the region $30 < N_{\text{smr}} < 50$, C is kept maximized and m_G is kept minimized, which implies that the ground-state contribution in $G(t)$ is maximally enhanced. Beyond this region, i.e., for $N_{\text{smr}} > 50$, since the size of the smeared operator exceeds the physical size of the glueball, C begins to decline and m_G begins to grow gradually.

The maximum overlap and the minimum mass should be achieved at almost the same N_{smear} . In fact, both of these two conditions should work as an indication of the maximally enhanced ground-state contribution. In practical calculations, these two conditions are achieved at slightly different N_{smear} . However, the numerical results on the pole-mass are almost the same. For instance, from Fig. 6, the former condition leads to $m_G(T = 130\text{MeV}) = 1482(25)$ MeV at $N_{\text{smear}} = 39$ and $m_G(T = 253\text{MeV}) =$

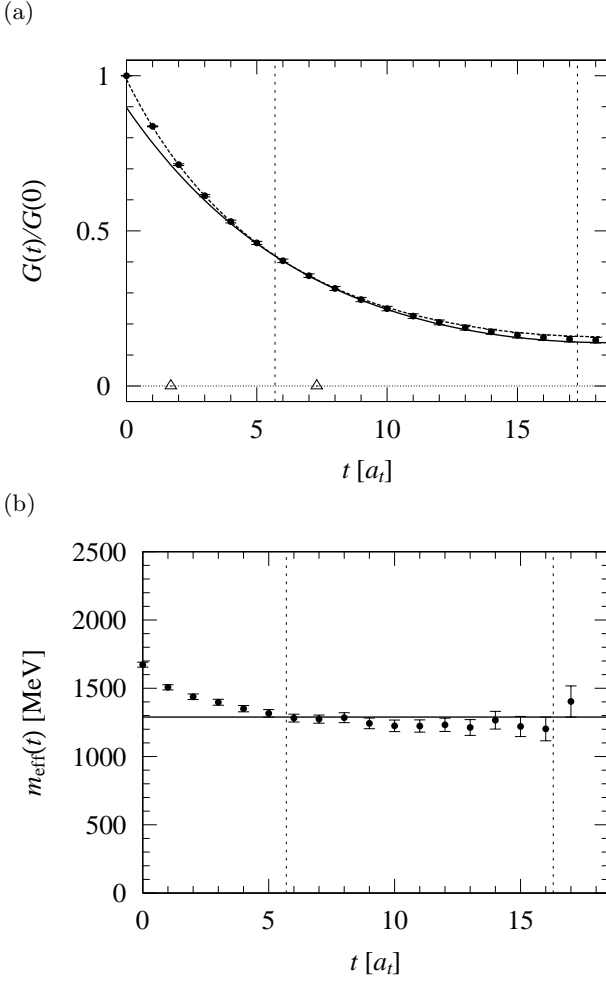


FIG. 5: (a) The temporal correlator $G(t)/G(0)$ of the 0^{++} glueball at the high temperature ($T = 253$ MeV) after the suitable smearing as Eq. (32). (b) The corresponding cosh-type effective-mass plot. The meaning of the solid lines and the dashed curve in (a) are the same as in Fig. 4. The errorbars are estimated with the jackknife analysis.

1294(26) MeV at $N_{\text{smear}} = 37$, while the latter condition leads to $m_G(T = 130\text{MeV}) = 1481(25)$ MeV at $N_{\text{smear}} = 41$ and $m_G(T = 253\text{MeV}) = 1284(27)$ MeV at $N_{\text{smear}} = 46$.

As we mentioned before, we divide the statistical data into the bins of the size 100 to reduce the possible auto-correlations. However, the bin-size dependence is not seen so strong even in the vicinity of the critical temperature T_c . Recall that the measurement interval of the gauge field configuration is 100 sweeps. Since this interval is already rather large, the bin-size of 100 seems to be sufficient to overcome the auto-correlations. This is also the case in the 2^{++} glueball.

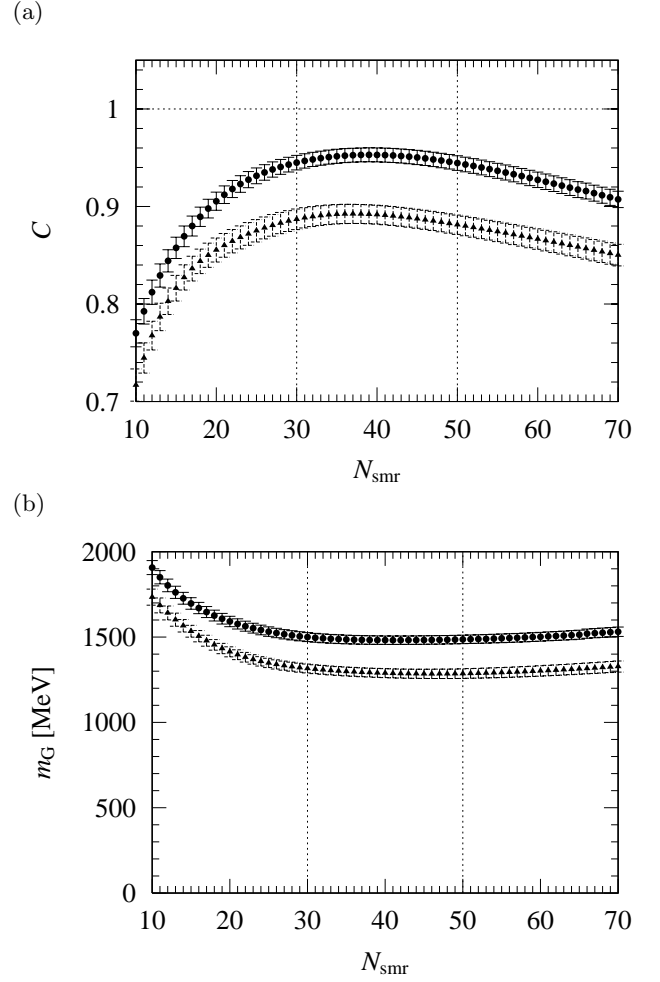


FIG. 6: (a) The ground-state overlap C and (b) the glueball mass m_G plotted against the smearing number N_{smr} for the temperatures $T = 130, 253$ MeV. The solid circle corresponds to $T = 130$ MeV, and the solid triangle to $T = 253$ MeV. The suitable smearing is found to be in the range as $30 < N_{\text{smr}} < 50$, where C is kept maximized and m_G is kept minimized simultaneously.

3. The main result on the pole mass

From the analysis at various temperatures as $T = 130, 187, 208, 218, 234, 246, 253, 260, 268, 275, 284$ MeV, we plot the SU(3) lattice QCD result for the pole-mass $m_G(T)$ of the lowest 0^{++} glueball against temperature T in Fig. 7. The solid circle and the cross denote the thermal glueball mass $m_G(T)$ obtained with the maximum overlap condition and the mass minimum condition, respectively. We see that they are almost the same. In Fig. 7, we observe a significant pole-mass reduction for the lowest 0^{++} glueball near T_c as

$$m_G(T) = 1200 \pm 100 \text{ MeV} \quad \text{for} \quad 0.9T_c < T < T_c, \\ m_G(T \simeq T_c) \simeq 1200 \text{ MeV}, \quad (42)$$

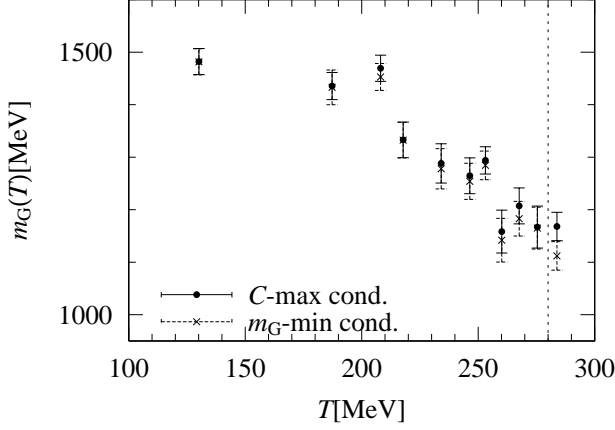


FIG. 7: The 0^{++} glueball mass $m_G(T)$ plotted against temperature T . The solid circle and the cross denote the thermal 0^{++} glueball mass obtained with the maximum overlap condition and the mass minimum condition, respectively. The vertical dotted line indicates the critical temperature $T_c \simeq 280$ MeV in quenched QCD.

in comparison with $m_G(T \simeq 0.5T_c) \simeq 1480$ MeV in our data or $m_G(T \sim 0) \simeq 1500$ – 1700 MeV in the lattice data in [21, 22, 23]. In this way, we observe nearly 300 MeV reduction or about 20 % reduction of the pole-mass of the lowest 0^{++} glueball in the vicinity of T_c as

$$\begin{aligned} m_G(T \sim 0) - m_G(T \simeq T_c) &\simeq 300 \text{ MeV}, \\ m_G(T \simeq T_c) &\simeq 0.8 m_G(T \sim 0). \end{aligned} \quad (43)$$

It is remarkable that the pole-mass shift obtained here is much larger than any other pole-mass shifts which has been ever observed in the meson sector in lattice QCD [13, 14].

We next consider the glueball size. To this end, we seek for N_{smr} , which realizes the maximum overlap condition. Such N_{smr} is listed in Table II for each temperature. By using Eq. (23), we give rough estimates of the thermal glueball sizes $\rho(T)$ at various temperatures, which are shown in Table II. We find

$$\rho \simeq 0.4 \text{ fm}, \quad (44)$$

both at low and high temperature below T_c .

In Table II, we summarize the lowest 0^{++} glueball mass $m_G(T)$, the ground-state overlap C^{max} , the correlated χ^2/N_{DF} , the fit-range (t_1, t_2) , the normalized overlap $g(0)$, the corresponding smearing number N_{smr} , the 0^{++} glueball size $\rho(T)$, and the number of gauge field configurations N_{conf} .

B. Thermal 2^{++} glueball

We show, in Figs. 8 (a) and 9 (a), the 2^{++} glueball correlators $G(t)/G(0)$ for $T = 130$ and 253 MeV,

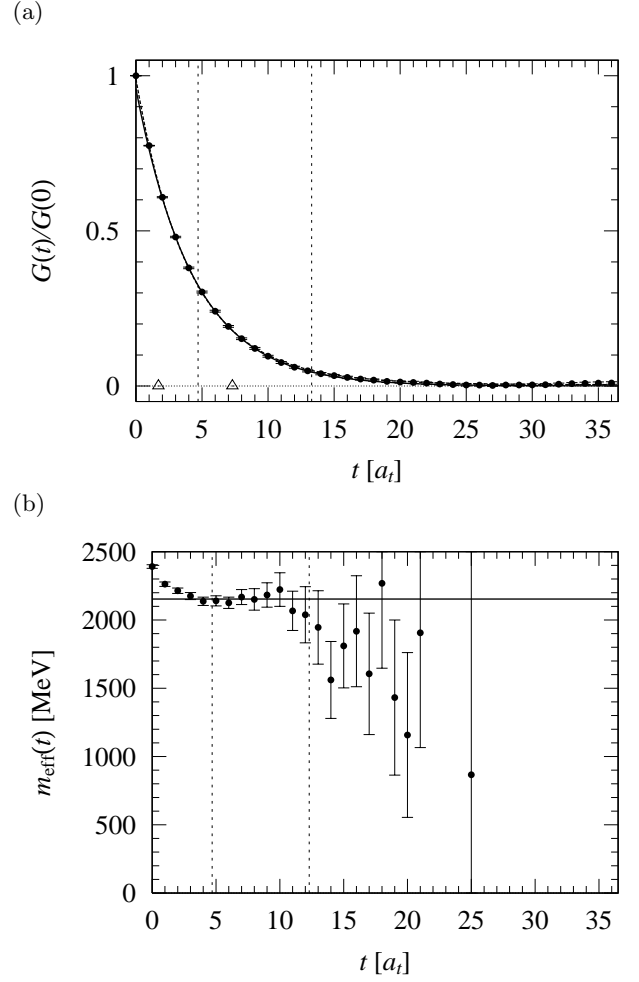


FIG. 8: (a) The 2^{++} glueball correlator $G(t)/G(0)$ of the at the low temperature ($T = 130$ MeV) after the suitable smearing as Eq. (32). (b) The corresponding cosh-type effective-mass plot. The meaning of the solid lines in both figures and the dashed curve in (a) are the same as in Fig. 4. In both figures, the errorbars are estimated with the jackknife analysis. In (b), the points beyond $t = 25$ are suppressed due to their huge statistical errors.

respectively, after the suitable smearings as Eq. (32). The solid lines denote the results of the best-fit analysis of single-cosh type. The fit-ranges are indicated by the vertical dotted lines, which are determined from the plateaus in the corresponding effective mass plots shown in Figs. 8 (b) and 9 (b).

From Fig. 8 (a), we find $C \simeq 0.96$ and $m_G \simeq 2154$ MeV for the 2^{++} glueball in low temperature case $T = 130$ MeV, which seems consistent with $m_G = 2000$ – 2400 MeV for the 2^{++} glueball at zero temperature [21]. From Fig. 9 (a), we find $C \simeq 0.90$ and $m_G \simeq 1996$ MeV for the 2^{++} glueball in the high temperature case $T = 253$ MeV ($< T_c$).

By combining the results at various temperatures, we plot the pole-mass of the thermal 2^{++} glueball against temperature in Fig. 10. The solid circle and the cross

TABLE II: The pole mass $m_G(T)$ of the lowest 0^{++} glueball at finite temperature T in SU(3) lattice QCD. The temperature T , the temporal lattice size N_t , the thermal glueball mass $m_G(T)$, the maximum ground-state overlap C^{\max} , the correlated χ^2/N_{DF} , the fit range (t_1, t_2) , the normalized ground-state overlap $g(0)$, the smearing number N_{smr} , the thermal glueball size $\rho(T)$ with Eq. (23), and the number the gauge configurations N_{conf} are listed. The best smearing on N_{smr} is determined with maximum overlap condition. Above $T_c \simeq 280$ MeV, the data such as m_G is to be understood as the best-fit parameters.

| $T[\text{MeV}]$ | N_t | $m_G[\text{MeV}]$ | C^{\max} | χ^2/N_{DF} | (t_1, t_2) | $g(0)$ | N_{smr} | $\rho[\text{fm}]$ | N_{conf} |
|-----------------|-------|-------------------|------------|------------------------|--------------|---------|------------------|-------------------|-------------------|
| 130 | 72 | 1482(25) | 0.95(1) | 1.60 | (5,14) | 0.95(1) | 39 | 0.43 | 5500 |
| 187 | 50 | 1436(26) | 0.94(1) | 0.60 | (5,25) | 0.94(1) | 41 | 0.44 | 5700 |
| 208 | 45 | 1469(25) | 0.96(1) | 0.73 | (5,22) | 0.96(1) | 36 | 0.41 | 6400 |
| 218 | 43 | 1333(34) | 0.89(1) | 1.22 | (7,21) | 0.89(1) | 41 | 0.44 | 9200 |
| 234 | 40 | 1288(37) | 0.87(2) | 1.01 | (8,20) | 0.87(2) | 36 | 0.41 | 8600 |
| 246 | 38 | 1265(34) | 0.88(1) | 1.21 | (7,13) | 0.88(1) | 39 | 0.43 | 8900 |
| 253 | 37 | 1294(26) | 0.89(1) | 1.45 | (6,17) | 0.90(1) | 37 | 0.41 | 8900 |
| 260 | 36 | 1158(41) | 0.80(2) | 1.54 | (10,17) | 0.81(2) | 42 | 0.44 | 9900 |
| 268 | 35 | 1207(34) | 0.85(1) | 1.96 | (7,16) | 0.86(1) | 36 | 0.41 | 8400 |
| 275 | 34 | 1167(40) | 0.81(2) | 0.22 | (9,12) | 0.82(2) | 44 | 0.45 | 8800 |
| 284 | 33 | 1168(27) | 0.82(1) | 1.01 | (8,16) | 0.83(1) | 41 | 0.44 | 9900 |
| 312 | 30 | 1158(28) | 0.79(2) | 1.22 | (8,15) | 0.80(2) | 45 | 0.46 | 9900 |
| 334 | 28 | 1090(42) | 0.75(2) | 1.56 | (8,14) | 0.78(2) | 40 | 0.43 | 5000 |
| 360 | 26 | 1289(27) | 0.85(1) | 1.90 | (6,13) | 0.87(1) | 34 | 0.40 | 5500 |
| 390 | 24 | 1215(33) | 0.79(2) | 0.91 | (8,12) | 0.83(2) | 32 | 0.39 | 7200 |

denote the pole-masses of the thermal 2^{++} glueball obtained with the maximum overlap condition and the mass minimum condition, respectively. We see again that they are qualitatively almost the same. The thermal 2^{++} glueball shows a tendency to decline by about 100 MeV for $T < 0.9T_c$, which is rather modest in contrast to the 0^{++} glueball. However, in the very vicinity of T_c , it shows a sudden reduction of about 500 MeV.

In Table III, we summarize the lowest 2^{++} glueball mass $m_G(T)$, the ground-state overlap C^{\max} , the correlated χ^2/N_{DF} , the fit-range (t_1, t_2) , the normalized overlap $g(0)$, the corresponding smearing number N_{smr} , the 2^{++} glueball size $\rho(T)$, and the number of gauge configurations N_{conf} .

C. Glueball correlations above T_c

In the deconfinement phase above T_c , neither hadrons nor glueballs are elementary excitations any more. Instead, quarks and gluons appear as elementary excitations in the quark gluon plasma. Therefore, we might wonder if there is anything interesting in investigating the color-singlet modes such as hadrons and glueballs above T_c . Nevertheless, based on the lattice-QCD Monte Carlo studies on the screening mass, it was pointed out that some of the strong correlations survive even above T_c in the scalar and pseudoscalar color-singlet modes such as σ and pions[12]. Hence, at least in the neighborhood of T_c , it may be possible that some of the nonperturbative effects survive in the deconfinement phase, which provides interesting information of the high-temperature QCD.

In this subsection, we attempt to examine the temporal correlator of the glueball-like color-singlet modes above T_c . We simply apply the pole-mass analysis

of the temporal correlators on the anisotropic lattice with $N_t = 24, 26, 28, 30, 33$, which correspond to $T = 284, 312, 334, 360, 390$ MeV, respectively. (A more sophisticated analysis will be performed in Sect. VI.)

We show, in Figs. 11, 12, the temporal correlators $G(t)/G(0)$ together with the associated effective masses $m_{\text{eff}}(t)$ at $T = 312, 390$ MeV, respectively, for the 0^{++} glueball-like color-singlet mode. In each effective-mass plot, a plateau is observed in the region indicated by the vertical dotted lines. By simply applying the single-cosh fit within the fit-range determined from the plateau, the “pole-mass” of the 0^{++} glueball is extracted above T_c , which is listed in Table II. We observe that the “pole-mass” is of about 1200 MeV, and that it changes rather continuously across the critical temperature T_c .

We perform the similar analysis for the 2^{++} glueball-like mode. In Figs. 13 and 14, the temporal correlators $G(t)/G(0)$ are plotted together with the associated effective mass plots at $T = 312, 390$ MeV, respectively. In each effective mass plot, we observe a plateau in the region, which is indicated by the vertical dotted lines. Similar to the 0^{++} case, we simply apply the single-cosh fit within the fit-range determined from the plateau to extract the “pole-mass”. The results are listed in Table III. We observe that the “pole-mass” is about 1400 MeV, and that its change is again rather continuous across the critical temperature T_c .

In both of these 0^{++} and 2^{++} cases, the size of the plateau tends to shrink at high temperatures above T_c . We note that, at much higher temperatures, the plateau finally disappears, which, however, seems to be due to the failure of the ground-state saturation in such a limited temporal size. At any rate, these phenomena suggest that the single-cosh ansatz becomes inappropriate for the fit-function of the temporal correlator $G(t)$ above T_c at

TABLE III: The pole mass $m_G(T)$ of the lowest 2^{++} glueball at finite temperature T in SU(3) lattice QCD. The meaning of T , N_t , $m_G(T)$, C^{\max} , χ^2/N_{DF} , (t_1, t_2) , $g(0)$, N_{smr} , R , and N_{conf} are the same as those in Table II. The best smearing on N_{smr} is determined with maximum overlap condition.

| $T[\text{MeV}]$ | N_t | $m_G[\text{MeV}]$ | C^{\max} | χ^2/N_{DF} | (t_1, t_2) | $g(0)$ | N_{smr} | $\rho[\text{fm}]$ | N_{conf} |
|-----------------|-------|-------------------|------------|------------------------|--------------|---------|------------------|-------------------|-------------------|
| 130 | 72 | 2167(35) | 0.97(1) | 1.01 | (5,13) | 0.97(1) | 54 | 0.50 | 5500 |
| 187 | 50 | 2123(39) | 0.95(2) | 0.57 | (5,13) | 0.95(2) | 39 | 0.43 | 5700 |
| 208 | 45 | 2054(58) | 0.90(3) | 1.07 | (7,19) | 0.90(3) | 47 | 0.47 | 6400 |
| 218 | 43 | 2146(55) | 0.91(3) | 1.49 | (7,12) | 0.91(3) | 68 | 0.56 | 9200 |
| 234 | 40 | 1986(72) | 0.85(4) | 1.03 | (8,14) | 0.85(4) | 63 | 0.54 | 8600 |
| 246 | 38 | 2142(55) | 0.95(3) | 0.33 | (6,14) | 0.95(3) | 41 | 0.44 | 8900 |
| 253 | 37 | 2009(47) | 0.90(2) | 1.32 | (6,13) | 0.90(2) | 38 | 0.42 | 8900 |
| 260 | 36 | 1928(46) | 0.88(2) | 3.12 | (6,12) | 0.88(2) | 52 | 0.49 | 9900 |
| 268 | 35 | 1919(71) | 0.87(4) | 1.53 | (8,16) | 0.87(4) | 43 | 0.45 | 8400 |
| 275 | 34 | 1572(62) | 0.68(4) | 0.91 | (9,14) | 0.68(4) | 51 | 0.49 | 8800 |
| 284 | 33 | 1466(78) | 0.60(5) | 1.51 | (11,16) | 0.60(5) | 51 | 0.49 | 9900 |
| 312 | 30 | 1319(58) | 0.61(4) | 0.33 | (10,15) | 0.62(4) | 53 | 0.50 | 9900 |
| 334 | 28 | 1427(57) | 0.69(3) | 1.41 | (8,14) | 0.70(3) | 46 | 0.46 | 5000 |
| 360 | 26 | 1482(43) | 0.76(2) | 0.69 | (7,13) | 0.78(2) | 62 | 0.54 | 5500 |
| 390 | 24 | 1484(56) | 0.69(4) | 1.65 | (8,12) | 0.71(4) | 32 | 0.39 | 7200 |

such a high temperature. However, because of the existence of the plateau in the effective-mass plot, we do not exclude so far the possibility that the color-singlet modes exist as meta-stable modes just above T_c . According to the lattice data, the color-singlet 0^{++} and 2^{++} modes have the pole-mass of about 1200 MeV and 1400 MeV, respectively, provided that it can be regarded as a bound state. However, even in this case, it should be kept in mind that such glueball-like modes can decay into two or more gluons in the quark-gluon-plasma phase. Since they cannot be stable above T_c , they will acquire finite decay widths. Hence, for more reliable analysis, it is necessary to take into account the effect of such a width, which will be attempted in Sect. VI.

V. DISCUSSION

In the previous section, we have studied the pole mass of the glueballs at finite temperature by analyzing the temporal correlators in SU(3) anisotropic lattice QCD. We have found the significant pole mass reduction of about 300 MeV in the vicinity of T_c or $m_G(T \simeq T_c)/m_G(T \sim 0) \simeq 0.8$ for the lowest 0^{++} glueball. In this section, we first compare our results with the related lattice QCD results on the screening masses as well as the pole masses of various hadrons at finite temperature. We discuss also the physical implications of our results, considering the phenomenological relation among the critical temperature, the pole-mass and the size of the thermal glueball by using a effective model of the QCD phase transition, i.e., the closed packing model. The section is closed with a consideration on what is the trigger of the QCD phase transition.

A. Comparison with the related lattice QCD results, the screening masses and the pole masses

Here, we compare our results with the related results on the mesonic pole-masses as well as the screening mass of various hadrons in lattice QCD at finite temperature.

We begin with the discussion of the pole-masses of mesons. The pole-masses of various mesons have been measured at finite temperature by using the anisotropic SU(3) lattice QCD at the quenched level in Refs. [13, 14]. From the same pole-mass analysis as ours, they have found that, both for light mesons and for heavy mesons such as the charmonium, the thermal pole-masses are almost unchanged from their zero-temperature values within the error bar below T_c . This tendency persists even in the vicinity of T_c as

$$m_{\text{meson}}(T) \simeq m_{\text{meson}}(T = 0), \quad \text{for } T \leq T_c. \quad (45)$$

In contrast, with the same pole-mass analysis, the lowest 0^{++} glueball shows the significant pole-mass reduction of about 300 MeV in the vicinity of T_c . Hence, the pole-mass reduction of the thermal 0^{++} glueball may serve as a better pre-critical phenomenon of the QCD phase transition at finite temperature than the pole-mass shifts of the thermal mesons, and the thermal glueball may become an interesting particle in the RHIC project in the future.

We next discuss the related results on the screening mass. The screening mass is defined as the reciprocal of the correlation length along the spatial direction. It can also reflect some of the important nonperturbative features of the QCD vacuum. Hence, it is also an interesting quantity, which may provide a signal of the QCD phase transition. However, unlike the pole-mass, which is considered to be directly measurable as a mass of an elementary excitation at finite temperature, the screening mass is not thought of as a directly measurable quantity

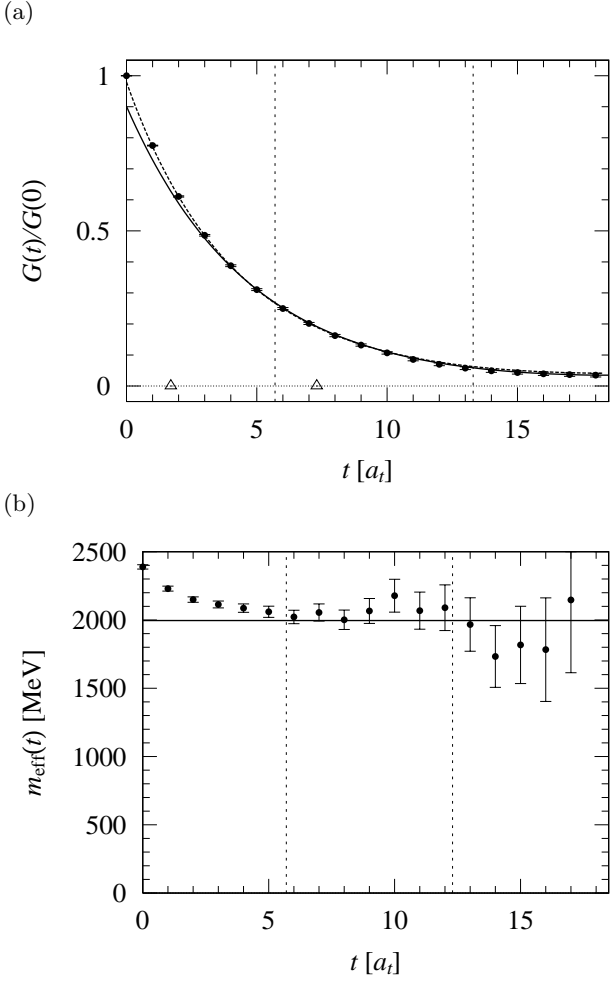


FIG. 9: (a) The 2^{++} glueball correlator $G(t)/G(0)$ at the high temperature ($T = 253$ MeV) after the suitable smearing as Eq. (32). (b) The corresponding cosh-type effective-mass plot. The meaning of the solid lines in both figures and the dashed curve in (a) are the same as in Fig. 4. In both figures, the errorbars are estimated with the jackknife analysis.

in high energy experiments. In the 0^{++} glueball sector, a significant reduction of the screening mass is reported as

$$m_G^{\text{scr}}(T = 0.75T_c)/m_G^{\text{scr}}(T \sim 0) = 0.6 \pm 0.1 \quad (46)$$

in SU(3) isotropic lattice QCD with $\beta_{\text{lat}} = 5.93$ over the lattice of the size $16^3 \times N_t$ with $N_t = 4, 6, 8$ at the quenched level [18, 19]. This significant reduction of the screening mass of the glueball would be an indication of the decrease of the nonperturbative nature of the QCD vacuum. In this sense, it seems to be consistent with our results on the significant reduction of the pole-mass of the thermal 0^{++} glueball near the critical temperature T_c . In contrast to the 0^{++} glueball, in the meson sector, the changes of the screening mass has been found again rather small below T_c at the quenched level [17].

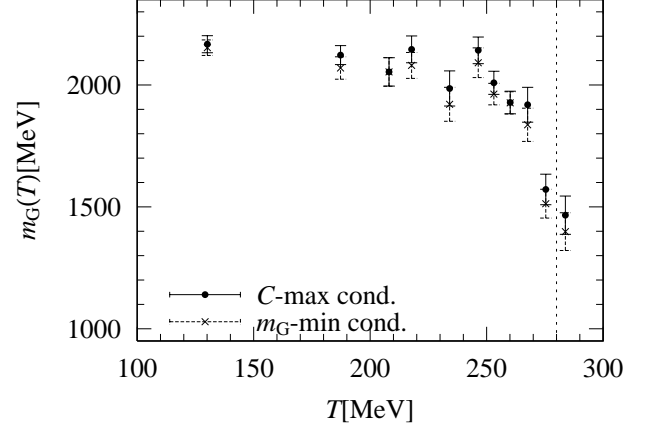


FIG. 10: The 2^{++} glueball mass plotted against temperature T . The solid circle and the cross denote the thermal 2^{++} glueball mass obtained with the maximum overlap condition and the mass minimum condition, respectively. The vertical dotted line indicates the critical temperature $T_c \simeq 280$ MeV in quenched QCD.

B. Analytic estimate of T_c with the closed packing model

Here, we analytically investigate the feature of the deconfinement phase transition, using a phenomenological effective model, the closed packing model. Our aim is to establish a phenomenological relation between the critical temperature T_c and the properties of the hadrons in order to appreciate the physical implications of our lattice QCD results.

In the closed packing model, hadrons are treated in the bag model picture. Therefore, each hadron has the intrinsic structure reflecting color confinement, and quarks and gluons are assumed to be confined inside a spherical bag with radius R . At low temperature, only a small number of such bags are thermally excited, and the thermodynamic properties of the system are described in terms of these spatially isolated bags, i.e., hadrons. With the increasing temperature T , the number $N(T)$ of the thermally excited bags increases. Gradually, these bags begin to overlap one another, and they finally cover the whole space region at the critical temperature T_c . Above T_c , since the volume of the outside disappears, the whole space is filled with liberated quarks and gluons, the thermodynamic properties of the system is now described in terms of these quarks and gluons. In this way, the QCD phase transition is described with the overlapping of the thermally excited bags in the closed packing model.

To proceed, we define the spatial occupation ratio $r_V(T)$ at temperature T as the ratio of the volume of the spatial regions inside the thermally excited bags to the volume V of the whole space region. In the closed packing model, $r_V(T)$ is the key quantity, which is esti-

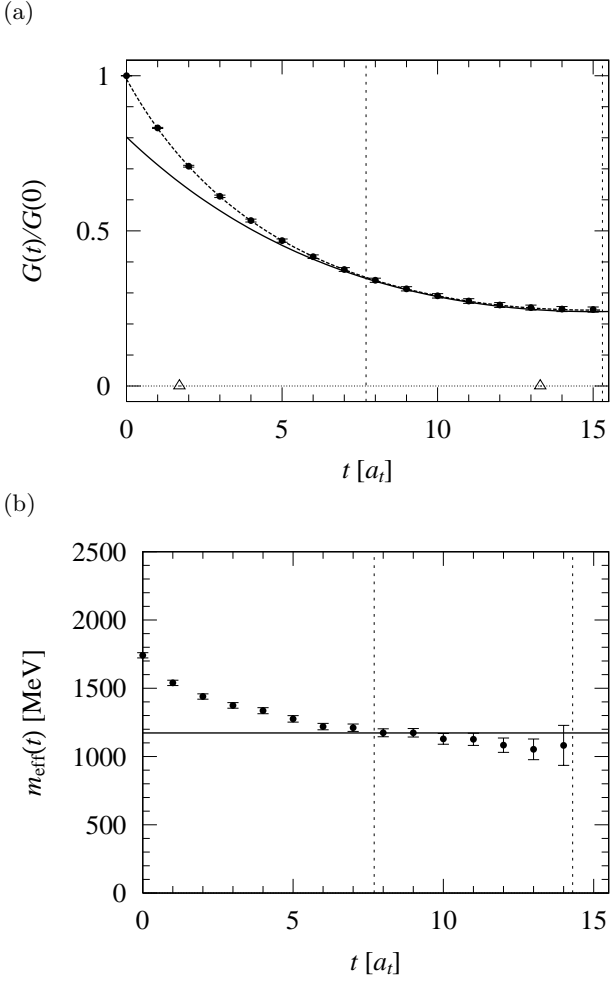


FIG. 11: (a) The 0^{++} glueball correlator $G(t)/G(0)$ at $T = 312$ MeV above T_c after the suitable smearing as Eq. (32). (b) The corresponding cosh-type effective-mass plot. The meaning of the solid lines in both figures and the dashed curve in (a) are the same as in Fig. 4. In both figures, the errorbars are estimated with the jackknife analysis.

mated as

$$r_V(T) = \frac{1}{V} \sum_n \frac{4\pi}{3} R_n^3 \times \lambda_n N_n(T) \quad (47)$$

$$= \sum_n \frac{4\pi}{3} R_n^3 \lambda_n \int \frac{d^3k}{(2\pi)^3} \frac{1}{e^{\sqrt{m_n^2 + k^2}/T} - 1},$$

where λ_n , m_n and R_n are the degeneracy, the mass and the bag radius of the n -th elementary excitation, respectively. As mentioned before, the QCD phase transition is expected to occur in the closed packing model, when the thermally excited bags almost cover the whole space region. Hence, the critical temperature T_c is estimated by solving

$$r_V(T_c) = 1. \quad (48)$$

In the ordinary context, the closed packing model is used to estimate the critical temperature of full QCD.

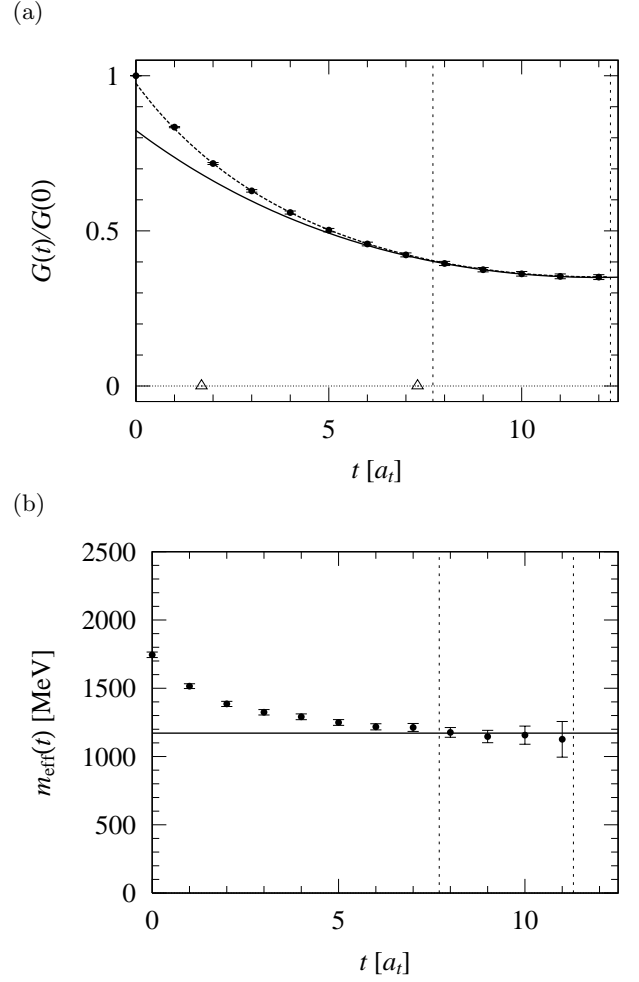


FIG. 12: (a) The 0^{++} glueball correlator $G(t)/G(0)$ at $T = 390$ MeV above T_c after the suitable smearing as Eq. (32). (b) The corresponding cosh-type effective-mass plot. The meaning of the solid lines in both figures and the dashed curve in (a) are the same as in Fig. 4. In both figures, the errorbars are estimated with the jackknife analysis.

In full QCD, the pion is the lightest physical excitation, and the other hadrons are all rather heavy, i.e., $m \gg m_\pi, T_c$. So the pion is expected to play the key role in describing the thermodynamic properties of full QCD in the confinement phase. Hence, we take account of only the pionic degrees of freedom in the closed packing model. By using the isospin degeneracy $\lambda = 3$, the mass $m = 140$ MeV and the radius $R \simeq 1$ fm as inputs, the critical temperature is estimated as $T_c \simeq 183$ MeV from Eq. (48), which seems to be successful in reproducing $T_c \simeq 170$ MeV in full lattice QCD.

We next apply the closed packing model to quenched QCD without quarks. In this case, the lightest physical excitation is the 0^{++} glueball with $m_G \simeq 1.5$ – 1.7 GeV, as the lattice QCD indicates. Following the similar argument as given above, we expect that the lowest 0^{++} glueball should play the key role in describing the thermodynamic properties of quenched QCD in the con-

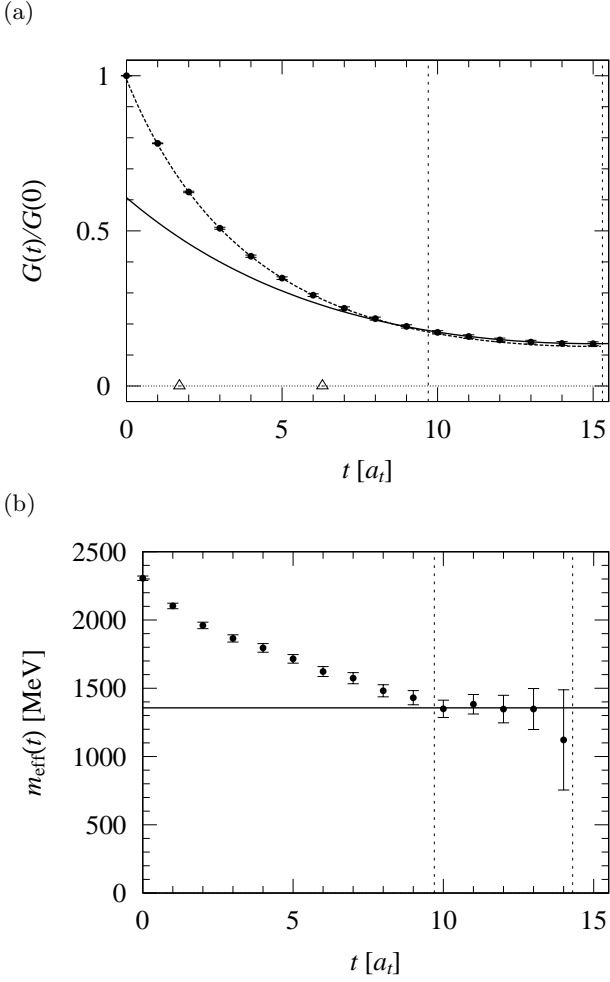


FIG. 13: (a) The 2^{++} glueball correlator $G(t)/G(0)$ at $T = 312$ MeV above T_c after the suitable smearing as Eq. (32). (b) The corresponding cosh-type effective-mass plot. The meaning of the solid lines in both figures and the dashed curve in (a) are the same as in Fig. 4. In both figures, the errorbars are estimated with the jackknife analysis.

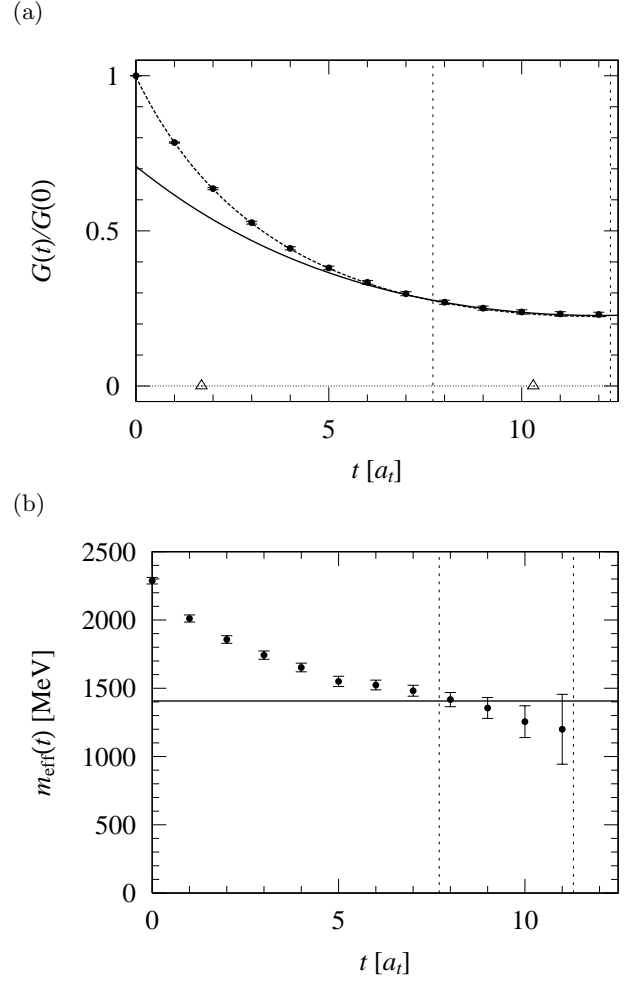


FIG. 14: (a) The 2^{++} glueball correlator $G(t)/G(0)$ at $T = 390$ MeV above T_c after the suitable smearing as Eq. (32). (b) The corresponding cosh-type effective-mass plot. The meaning of the solid lines in both figures and the dashed curve in (a) are the same as in Fig. 4. In both figures, the errorbars are estimated with the jackknife analysis.

finement phase. Hence, we consider only the thermal contribution of the 0^{++} glueball in the closed packing model.

As for the size of the lowest 0^{++} glueball, we have estimated as $\rho \sim 0.4$ fm from the lattice QCD analysis with the smearing method, as shown in Table II. However, since there is no established value so far for the glueball size, we adopt a rather wide range as $R = 0.5\text{--}1$ fm. With the degeneracy $\lambda = 1$, the mass $m \simeq 1500\text{--}1700$ MeV, and $R \simeq 0.5\text{--}1$ fm, we obtain $T_c \simeq 440\text{--}705$ MeV from Eq. (48).

In Fig. 15, we show the relation among the critical temperature T_c , the glueball mass m and the glueball size R in the closed packing model. All of these data indicate that the closed packing model gives too high values in comparison with the quenched lattice QCD result, $T_c \simeq 260$ MeV.

In order to improve the value of T_c , we include the

thermal contributions from the excited glueball states. As is easily seen from Eq. (47), the effect of such inclusions is to increase the value of $r_V(T)$, which therefore leads to lowering the critical temperature T_c . We include all the glueballs predicted in the quenched lattice QCD simulations [21], $0^{++}(1730)$, $2^{++}(2400)$, $0^{-+}(2590)$, $0^{*++}(2670)$, $1^{+-}(2940)$, $2^{-+}(3100)$, $3^{+-}(3550)$, $0^{*-+}(3640)$, $3^{++}(3690)$, $1^{--}(3850)$, $2^{*-+}(3890)$, $2^{--}(3930)$, $3^{--}(4130)$, $2^{+-}(4140)$, $0^{+-}(4740)$. While $2^{++}(2400)$ mode gives a sizable correction to T_c as $T_c \simeq 404\text{--}559$ MeV, the other modes give much smaller contributions—they are too heavy to give any significant contributions. Even after the inclusion of all of these contributions, we still obtain rather large values of T_c as $T_c(R = 1\text{fm}) \simeq 380$ MeV, $T_c(R = 0.5\text{fm}) \simeq 495$ MeV.

These failures originate from the huge difference between $T_c \simeq 260$ MeV and $m_G \simeq 1500\text{--}1700$ MeV, i.e., $m_G \gg T_c$. In contrast with full QCD where $m_\pi \sim$

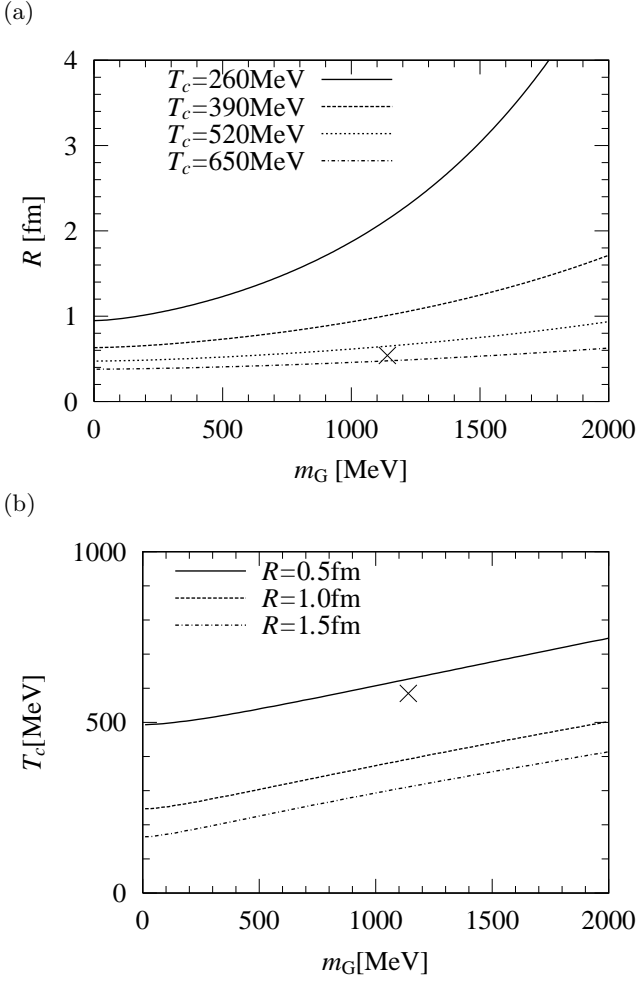


FIG. 15: (a) The critical temperature T_c shown as a function of the glueball mass m_G and the glueball radius R in the closed packing model. The cross symbol (\times) denotes the lattice QCD data for the pole mass $m(T)$ and the radius $R(T)$ ($= \rho(T)$) of the lowest glueball mass near T_c . (b) The critical temperature T_c plotted against the glueball mass m_G assuming various glueball radii R .

$T_c(\text{full})$, the elementary excitations in quenched QCD are heavy glueballs only. Hence, their thermal contributions are strongly suppressed by the extremely small statistical factor as

$$\exp \left[-\sqrt{m_G^2 + \vec{k}^2}/T \right] \leq e^{-m_G/T_c} \simeq 0.0014, \quad (49)$$

even in the neighborhood of $T_c(\text{quenched}) \sim 260$ MeV.

The possible resolution may be found in either a considerable reduction of the pole-mass of the lowest 0^{++} glueball near T_c as $m_G(T \simeq T_c) \sim T_c(\text{quenched}) \simeq 260$ MeV or a tremendous swelling of the lowest 0^{++} glueball near T_c as $R(T \simeq T_c) \gg 1$ fm. However, the lattice QCD results obtained in the last section show that the thermal 0^{++} glueball persists to hold still a rather large pole-mass as $m(T \simeq T_c) \simeq 1200$ MeV, while its size remains unchanged as $\rho(T \simeq T_c) \simeq \rho(T \sim 0) \simeq 0.4$ fm. The

cross symbol (\times) in Fig. 15 indicates the lattice QCD data of the pole-mass $m_G(T)$ and the size $\rho(T)$ near T_c . We find again a large value of the critical temperature as $T_c \simeq 600$ MeV, from the closed packing model analysis by using the lattice QCD data of the pole-mass and the size of the thermal glueball as inputs. In the next subsection, we discuss the physical implications of this problem, considering the trigger of the QCD phase transition.

C. The trigger of the QCD phase transition

The lattice QCD results obtained in the last section indicate that the lowest 0^{++} glueball exhibits the significant pole-mass reduction of about 300 MeV in the vicinity of T_c , while its size remains almost unchanged. Although this pole-mass reduction is significant, the lowest 0^{++} glueball still holds a rather large pole-mass, which is larger than 1 GeV even near T_c . Here, we discuss its physical consequence and consider the trigger of the QCD phase transition.

As was mentioned before, the lowest 0^{++} glueball is the lightest physical excitation in the quenched QCD below T_c . Hence, its thermal behavior is expected to be of primary relevance at finite temperature. However, since our lattice QCD results indicate $m_G > 1$ GeV even near T_c , the thermodynamical contribution of the 0^{++} glueball is expected to be strongly suppressed due to the small statistical factor as $e^{-m_G/T}$ for $T \leq T_c \simeq 260$ MeV [15]. Hence, the thermal glueball excitation may play less relevant roles in the deconfinement phase transition than we have expected naively based on the closed packing model. If this is the case, what is the driving force to bring the deconfinement phase transition? In this way, our result brings up an interesting new puzzle on the QCD phase transition.

In the last subsection, we have seen that the closed packing model for pions successfully reproduces the critical temperature $T_c(\text{full}) \simeq 140$ MeV of a full lattice QCD result. However, there does exist a similar problem concerning the smallness of T_c also in full QCD. Recall that, in the actual lattice QCD calculations, the pion mass is taken to be still rather heavy as $m_\pi > 400$ MeV. It follows that the thermal excitation of pions is expected to be suppressed even in the vicinity of the critical temperature $T_c(\text{full}) \simeq 170$ MeV. Hence, we may wonder what is the essential reason to obtain such a small value of T_c . In addition, T_c seems rather insensitive to the value of the pion mass m_π in full lattice QCD, which seems to be in contradiction with the strong m_π dependence in the Boltzmann factor $e^{-m_\pi/T}$. These facts may indicate that the role of the thermal pions in the thermodynamical properties of full QCD is less relevant than we have expected naively based on the closed packing model. In this way, this puzzle seems rather general for the QCD phase transition at finite temperature.

VI. NEW ANALYSIS OF TEMPORAL CORRELATIONS —SPECTRAL FUNCTION

In this section, we attempt to generalize the pole-mass analysis given in Sect. IV. Our aim is to analyze our lattice QCD data of the temporal correlator $G(t)/G(0)$ without assuming the narrowness of the thermal width of the bound-state peak in the spectral function. We first consider the functional form of the new fit-function, which takes into account the effect of the thermal width. We also provide its theoretical background. We then present the numerical results of this new analysis. At the end of the section, we consider the relation between this new analysis and the single-cosh analysis given in Sect. IV.

A. Theoretical consideration on the temporal correlator and the Breit-Wigner fit-function

In Sect. IV, we have presented the results of the pole-masses of the thermal 0^{++} and 2^{++} glueballs at finite temperature obtained in the best-fit analysis of the temporal correlator $G(t)/G(0)$ with the fit function of the single-cosh type. In this analysis, we have regarded each thermal glueball as a quasi-particle and have assumed that the thermal width of the corresponding peak is sufficiently narrow in the spectral function. In this case, the ground-state contribution to the spectral function can be well approximated as $\rho(\omega) \simeq 2\pi\{\delta(\omega - m_G(T)) - \delta(\omega + m_G(T))\}$ by introducing the temperature-dependent pole-mass $m_G(T)$ of the thermal glueball. As a consequence, in order to measure the pole-mass, we can adopt the standard single hyperbolic cosine in Eq. (38) as the fit function, and perform the best-fit analysis in exactly the same way as the zero-temperature case.

However, to be strict, at finite temperature, each bound-state peak in the spectral function $\rho(\omega)$ acquires a non-zero width through the thermal fluctuations. Since the thermal width would grow with the temperature, it is expected to play the more significant roles and become the less negligible at the higher temperature. Hence, it is desirable to take into account the effect of the thermal width in the best-fit analysis. We can directly see how such a thermal width $\Gamma(T)$ affects the temporal correlator $G(t)$ in the spectral representation as

$$G(t) = \int_{-\infty}^{\infty} \frac{d\omega}{2\pi} \frac{\rho(\omega)}{2 \sinh(\beta\omega/2)} \cosh(\omega(\beta/2 - t)). \quad (50)$$

There may have already appeared a signal of such a non-zero thermal width in the glueball correlators in Figs. 4, 5, 11, 12, where the ground-state enhancement works the less effective for the higher temperature. In Table II, we observe a tendency that $g(0)$ declines with the increasing temperature. For instance, $g(0) \simeq 0.95$ for the low temperature $T = 130$ MeV becomes $g(0) \lesssim 0.90$ for the higher temperature $T \gtrsim 250$ MeV for the 0^{++}

glueball. In the effective-mass plots in Figs. 4, 5, 11, we observe that the plateau tends to start with the larger t at the higher temperature. These phenomena may indicate that the existence of the other spectral components become the less negligible at the higher temperature.

In fact, at finite temperature, each bound state peak acquires a thermal width. The thermal width is one of the most feasible candidates for the source of these other spectral components, since the contributions from such a bunch of spectral components cannot be well separated even by means of the smearing procedure. In this section, we perform a more general new analysis of the temporal correlator $G(t)/G(0)$ as an attempt to take into account the effects of the thermal width $\Gamma(T)$ of the ground-state peak in the spectral function $\rho(\omega)$.

At zero temperature, the bound-state poles of the Green functions $G_R(\omega)$ and $G_A(\omega)$ in Eq. (9) lie on the real axis in the complex ω -plane. Hence, the lowest-state contribution to the spectral function $\rho(\omega)$ is expressed as $\rho(\omega) = 2\pi A \{\delta(\omega - m_G) - \delta(\omega + m_G)\}$, where A and m_G are the strength and the mass of the lowest-state pole, respectively. By inserting this expression into Eq. (50), and taking the limit $\beta = 1/T \rightarrow \infty$, we recover the familiar expression as

$$\begin{aligned} G(t) &= \lim_{\beta \rightarrow \infty} A \frac{\cosh(m_G(\beta/2 - t))}{\sinh(\beta m_G/2)} \\ &= A \exp(-m_G t). \end{aligned} \quad (51)$$

With the increasing temperature, these bound-state poles are moving off the real axis into the second Riemannian sheet of the complex ω -plane. Suppose that the ground-state pole is located at $\omega = \omega_0 + i\Gamma$ ($\omega_0, \Gamma \in \mathbb{R}$) in the second Riemannian sheet. Since the spectral function $\rho(\omega)$ is the imaginary part of the Green function, the ground-state contribution in the spectral function $\rho(\omega)$ can be expressed in the following way:

$$\begin{aligned} \rho(\omega) &= \text{Im}(G_R(\omega)) \\ &= 2\pi A \left(\delta_\Gamma(\omega - \omega_0) - \delta_\Gamma(\omega + \omega_0) \right) + \dots \end{aligned} \quad (52)$$

Here, A represents the residue of the pole, $\delta_\epsilon(x)$ denotes the Lorentzian at $x = 0$ with the width ϵ (> 0), which is defined as

$$\begin{aligned} \delta_\epsilon(x) &\equiv \frac{1}{\pi} \text{Im} \left(\frac{1}{x - i\epsilon} \right) \\ &= \frac{1}{\pi} \frac{\epsilon}{x^2 + \epsilon^2}. \end{aligned} \quad (53)$$

The appearance of the second term in Eq. (52) is due to the fact that the spectral function $\rho(\omega)$ is an odd function in ω , reflecting the bosonic nature of the glueball. “ \dots ” in Eq. (52) represents the contributions from the excited states, which are expected to be suppressed after the appropriate smearing procedure. Corresponding to Eq. (52), the ground state contribution in the temporal

glueball correlator $G(t)$ is expressed as

$$G(t) = \int_{-\infty}^{\infty} \frac{d\omega}{2\pi} \frac{\cosh(\omega(\beta/2 - t))}{\sinh(\beta\omega/2)} \times 2\pi A \left(\delta_{\Gamma}(\omega - \omega_0) - \delta_{\Gamma}(\omega + \omega_0) \right) + \dots \quad (54)$$

Hence, to extract the center $\omega_0(T)$ and the thermal width $\Gamma(T)$ of the lowest-state peak in $G(t)/G(0)$, the appropriate fit-function is given as

$$g_{\Gamma}(t) \equiv \int_{-\infty}^{\infty} \frac{d\omega}{2\pi} \frac{\cosh(\omega(\beta/2 - t))}{\sinh(\beta\omega/2)} \times 2\pi \tilde{A} \left(\delta_{\Gamma}(\omega - \omega_0) - \delta_{\Gamma}(\omega + \omega_0) \right), \quad (55)$$

where \tilde{A} , ω_0 and the Γ are used as the fit parameters. Here, \tilde{A} corresponds to $A/G(0)$ in Eq. (54), and will be

referred to as the strength parameter. We will refer to Eq. (55) as the fit-function of “Breit-Wigner” type. Note that $g_{\Gamma}(t)$ is a generalization of the fit-function $g(t)$ of the single-cosh type in the sense that $g_{\Gamma}(t)$ reduces to $g(t)$ in a special limit as

$$\lim_{\Gamma \rightarrow +0} g_{\Gamma}(t) = g(t). \quad (56)$$

In this sense, the best-fit analysis of Breit-Wigner type serves as a generalization of the ordinary pole-mass analysis of single-cosh type. Note that the analysis of Breit-Wigner type is rather general, which is also applicable to the temporal correlators of various thermal hadrons.

We note that, after some calculations, the fit-function $g_{\Gamma}(t)$ in Eq. (55) can be expressed as the infinite series as

$$g_{\Gamma}(t) = \tilde{A} \left[\text{Re} \left(\frac{\cosh \{(\omega_0 + i\Gamma)t\}}{\sinh \left\{ \frac{\beta}{2}(\omega_0 + i\Gamma) \right\}} \right) + 2\beta\omega_0 \sum_{n=1}^{\infty} \cos \left(\frac{2\pi n}{\beta} t \right) \left\{ \frac{1}{(2\pi n + \beta\Gamma)^2 + \beta^2\omega_0^2} - (n \rightarrow -n) \right\} \right] \quad (57)$$

We make a comment on the role of the smearing method in the presence of the non-zero width of the lowest state (or the ground state) peak at finite temperature. As was explained in Sect. II, the smearing method aims at a suitable choice of the glueball operators, by providing a series of operators with different sizes, all of which, however, hold the identical quantum numbers in common. Whereas the residues of the bound-state poles are affected by the different choices of the glueball operators, their positions in the complex ω -plane are not affected. One can thereby enhance the residue of the particular bound-state pole by a clever choice of the operator, while keeping its position unaffected. Note that the position of the pole determines the characteristics of the peak, i.e., the center and the width. As this clever choice of the operator, we will use the smearing method, which is expected to pick up and then to enhance the contribution of the ground-state peak.

B. Setup for the Breit-Wigner fit analysis

In this subsection, we consider the fit-range of the Breit-Wigner fit analysis for the temporal glueball correlator $G(t)$. We examine also the N_{smr} -dependence of the best-fit parameters in order to estimate the systematic error originating from a particular choice of N_{smr} .

1. The fit range

We consider the determination of the fit-range of the Breit-Wigner fit analysis. As a consequence of the smearing method, the contribution from the ground-state peak is expected to be enhanced in the spectral function $\rho(\omega)$. However, even with the smearing method, the complete elimination of all the excited-state contributions is practically impossible. Therefore, we have to reduce further the remaining contributions from the higher spectral components as much as possible. To this end, we seek for the appropriate fit-range, where $G(t)$ consists of nearly a single-peak contribution. We adopt the strategy, which is a straightforward extension to the one adopted in the single-cosh analysis, i.e., the analysis based on the effective-mass plot in the following way. We consider the “effective center” $\omega_{0;\text{eff}}(t)$ and the “effective width” $\Gamma_{\text{eff}}(t)$, which are defined as the solutions to the following equations:

$$\begin{aligned} G(t)/G(t+1) &= g_{\Gamma}(t)/g_{\Gamma}(t+1) \\ G(t+1)/G(t+2) &= g_{\Gamma}(t+1)/g_{\Gamma}(t+2), \end{aligned} \quad (58)$$

for given $G(t)/G(t+1)$ and $G(t+1)/G(t+2)$ at each fixed t . In Fig. 16, we show the plots of the effective centers $\omega_{0;\text{eff}}(t)$ and the effective width $\Gamma_{\text{eff}}(t)$ of the 0^{++} glueball correlators at various temperatures $T = 130, 253, 390$ MeV. The statistical errors for $\omega_{0;\text{eff}}(t)$ and $\Gamma_{\text{eff}}(t)$ are estimated with the jackknife analysis. In each pair of $\omega_{0;\text{eff}}(t)$ and $\Gamma_{\text{eff}}(t)$ plots, there appears a simultaneous plateau, a region where $\omega_{0;\text{eff}}(t)$ and $\Gamma_{\text{eff}}(t)$ are almost

constant simultaneously. In this region, $G(t)$ is expected to consist of a single peak contribution, and $g_\Gamma(t)$ can properly represent the contribution of the ground-state peak in Eq. (54). Note that a nontrivial t -dependence implies the existence of the contributions from the other spectral components. In this sense, the existence of the simultaneous plateau in the pair of $\omega_{0;\text{eff}}(t)$ and $\Gamma_{\text{eff}}(t)$ plots works as a necessary condition to determine whether the fit function $g_\Gamma(t)$ of Breit-Wigner type is appropriate or not.

2. The N_{smr} dependence

We consider the N_{smr} -dependences of the best-fit parameters, the center $\omega_0(T)$ and the thermal width $\Gamma(T)$ of the lowest peak. Since the physical meaning of \tilde{A} is not so obvious in the presence of the thermal width, we consider $g_\Gamma(0)$ instead of \tilde{A} . Note that $g_\Gamma(0)$ is a generalization of $g(0)$ in the single-cosh analysis. We will refer to $g_\Gamma(0)$ as the “normalized overlap” with the state corresponding to the lowest peak.

In Fig. 17, the normalized overlap $g_\Gamma(0)$, the center $\omega_0(T)$ and the thermal width $\Gamma(T)$ are plotted against N_{smr} for fixed $\alpha = 2.1$ at $T = 130$ and 253 MeV below T_c with circles and triangles, respectively. In the region of $30 \leq N_{\text{smr}} \leq 50$, $g_\Gamma(0)$ is maximized, and $\omega_0(T)$ and $\Gamma(T)$ are minimized. These behaviors of $g_\Gamma(0)$ and $\omega_0(T)$ are analogous to those of the normalized overlap $g(0)$ (or the overlap C) and the pole-mass $m_G(T)$ in the single-cosh analysis. As for the thermal width $\Gamma(T)$, since the contamination of the higher spectral components is expected to make it wider, the minimal $\Gamma(T)$ would characterize the lowest-peak saturation.

According to these considerations, we expect that the lowest-peak contribution is maximally enhanced in the region of $30 \leq N_{\text{smr}} \leq 50$, and that the normalized overlap $g_\Gamma(0) \simeq 1$ provides a saturation rate of the lowest-peak contribution, in exactly the same way as $g(0) \simeq 1$ does in the single-cosh analysis. Note that both for the center ω_0 and the thermal width Γ , the N_{smr} -dependence is rather small in the region of $30 \leq N_{\text{smr}} \leq 50$, resulting in the small systematic error on the specific choice of N_{smr} . The behaviors are qualitatively the same at the other temperatures below T_c . This is also the case for the 2^{++} glueball.

In contrast, qualitatively different behaviors appear above T_c . In Fig. 18, the normalized overlap $g_\Gamma(0)$, the center ω_0 and the thermal width Γ are plotted against N_{smr} for $\alpha = 2.1$ at $T = 312$ and 390 MeV above T_c with the square and the diamond, respectively. We see that the overlap $g_\Gamma(0)$ becomes too insensitive to N_{smr} to determine its maximum. In some cases, it does not take the maximum in the region $N_{\text{smr}} < 70$. In addition, there are sizable N_{smr} -dependences in ω_0 and Γ in this region, although Γ seem to take its minimum around the typical smearing number as $N_{\text{smr}} \sim 40$. As for the center ω_0 , it continues to decline and does not take the minimum

in the region $N_{\text{smr}} < 70$. We note that qualitatively the same behaviors are observed in the 2^{++} channel. Considering these behaviors, it would be better to consider the Breit-Wigner analysis in both cases with $N_{\text{smr}} = 40$ and N_{smr} which maximizes $g_\Gamma(0)$ above T_c .

In this section, unless otherwise stated, we adopt the smearing with $\alpha = 2.1$ and $N_{\text{smr}} = 40$, which is one of the most suitable pair of the smearing parameters. Only for the accurate measurement, we seek for such N_{smr} , which maximizes the overlap $g_\Gamma(0)$.

3. The smearing and the single-pole saturation

In this section, we use the smearing method to enhance the residues of the pair of the complex poles associated with the low-lying peak. However, in the presence of the non-zero thermal width, the meaning of the “low-lying” contribution may become less definite in a strict sense, since these peaks can overlap with each other. With the increasing temperature, the thermal width becomes wider. Hence, each bound-state peak becomes less distinguishable from one another due to the possibly strong overlap with the neighboring peaks. In some cases, one may wonder if the smearing really extract only the contribution from the lowest-state peak among the overlapping peaks. Therefore, we have to check the smallness of the excited-state contamination by examining the quality of the fitting of $G(t)/G(0)$ with $g_\Gamma(t)$. If $G(t)/G(0)$ can be well fitted with $g_\Gamma(t)$, we may expect that the smearing works so that the lowest-state can dominate in the spectral function $\rho(\omega)$.

C. Numerical results of the Breit-Wigner fit

In this subsection, we perform the Breit-Wigner fit analysis for the lattice QCD data of the temporal glueball correlator. We also present the numerical results on the spectral function of the glueballs at various temperatures. Finally, we consider the relation between the single-cosh analysis and the Breit-Wigner analysis.

1. The glueball correlators

In Figs. 4 (a), 5 (a), 11 (a), 12 (a), we show the best-fit function $g_\Gamma(t)$ for the 0^{++} glueball correlator $G(t)/G(0)$ with dashed curves at various temperatures as $T = 130, 253, 312, 390$ MeV, respectively. Similarly for the 2^{++} glueball, in Figs. 8 (a), 9 (a), 13 (a), 14 (a), the best-fit functions $g_\Gamma(t)$ are added with dashed curves at various temperatures as $T = 130, 253, 312, 390$ MeV, respectively. It is remarkable that, at all of these temperatures, the lattice QCD data of the temporal glueball correlators $G(t)/G(0)$ are in a good agreement with $g_\Gamma(t)$ in the whole region of t .

TABLE IV: The analysis of the temporal correlator $G(t)/G(0)$ of the thermal 0^{++} glueball based on Breit-Wigner ansatz of the spectral function $\rho(\omega)$ as Eq. (52). The temperature T , the temporal lattice size N_t , the center ω_0 , the width Γ and the strength parameter \tilde{A} of the peak, the correlated χ^2/N_{DF} , the fit-range (t_1, t_2) , the overlap $g_\Gamma(0)$, the smearing number N_{smr} which achieves the $g_\Gamma(0)$ -max condition, and the gauge configuration number N_{conf} are listed. The asterisk “*” in the column of N_{smr} indicates that the original value of N_{smr} is 70, which had been replaced by the suitable smearing number 40. We had done this, because $N_{\text{smr}} = 70$ is the end point and because the situation similar to the one in Fig. 18 at $T = 390$ is observed.

| $T[\text{MeV}]$ | N_t | $\omega_0[\text{MeV}]$ | $\Gamma[\text{MeV}]$ | \tilde{A} | χ^2/N_{DF} | (t_1, t_2) | $g_\Gamma(0)$ | N_{smr} | N_{conf} |
|-----------------|-------|------------------------|----------------------|-------------|------------------------|--------------|---------------|------------------|-------------------|
| 130 | 72 | 1525(19) | 126(42) | 1.03(2) | 0.14 | (2, 8) | 0.979(3) | 41 | 5500 |
| 187 | 50 | 1532(20) | 165(42) | 1.04(2) | 0.65 | (2,16) | 0.977(3) | 34 | 5700 |
| 208 | 45 | 1548(22) | 165(45) | 1.05(2) | 1.48 | (2, 9) | 0.985(3) | 33 | 6400 |
| 218 | 43 | 1547(22) | 302(55) | 1.11(3) | 0.94 | (3, 8) | 0.992(6) | 31 | 9200 |
| 234 | 40 | 1476(21) | 279(48) | 1.09(2) | 1.23 | (2, 6) | 0.988(3) | 42 | 8600 |
| 246 | 38 | 1467(22) | 323(46) | 1.11(2) | 0.37 | (2, 9) | 0.990(3) | 37 | 8900 |
| 253 | 37 | 1471(20) | 339(47) | 1.11(2) | 0.53 | (2, 7) | 0.988(3) | 40 | 8900 |
| 260 | 36 | 1418(26) | 284(50) | 1.07(3) | 0.18 | (3,10) | 0.976(5) | 42 | 9900 |
| 268 | 35 | 1443(27) | 423(59) | 1.15(3) | 0.57 | (2, 8) | 0.991(4) | 37 | 8400 |
| 275 | 34 | 1457(28) | 327(73) | 1.09(4) | 0.79 | (3, 8) | 0.978(8) | 35 | 8800 |
| 284 | 33 | 1432(19) | 484(52) | 1.17(3) | 1.89 | (2,10) | 0.988(3) | 45 | 9900 |
| 312 | 30 | 1471(23) | 603(54) | 1.21(3) | 1.40 | (2,13) | 0.989(4) | 46 | 9900 |
| 334 | 28 | 1360(56) | 940(110) | 1.44(10) | 1.11 | (2,12) | 1.002(6) | 50 | 5000 |
| 360 | 26 | 1531(41) | 786(123) | 1.27(8) | 1.41 | (2, 6) | 0.994(7) | 32 | 5500 |
| 390 | 24 | 1446(22) | 611(82) | 1.14(5) | 0.62 | (2, 7) | 0.976(5) | 40* | 7200 |

TABLE V: The analysis of the thermal 2^{++} glueball correlator $G(t)/G(0)$ with Breit-Wigner ansatz of the spectral function $\rho(\omega)$. The meaning of T , N_t , ω_0 , Γ , \tilde{A} , χ^2/N_{DF} , (t_1, t_2) , $g_\Gamma(0)$ and N_{conf} are the same as those in Table IV. The suitable smearing with Eq. (32) is adopted.

| $T[\text{MeV}]$ | N_t | $\omega_0[\text{MeV}]$ | $\Gamma[\text{MeV}]$ | \tilde{A} | χ^2/N_{DF} | (t_1, t_2) | $g_\Gamma(0)$ | N_{smr} | N_{conf} |
|-----------------|-------|------------------------|----------------------|-------------|------------------------|--------------|---------------|------------------|-------------------|
| 130 | 72 | 2250(21) | 182(60) | 1.04(2) | 1.23 | (2, 7) | 0.989(5) | 39 | 5500 |
| 187 | 50 | 2182(28) | 131(70) | 1.02(3) | 0.59 | (2,10) | 0.980(7) | 48 | 5700 |
| 208 | 45 | 2233(26) | 148(76) | 1.02(3) | 1.21 | (2, 6) | 0.983(7) | 47 | 6400 |
| 218 | 43 | 2224(21) | 88(44) | 1.00(2) | 1.42 | (2,10) | 0.978(4) | 49 | 9200 |
| 234 | 40 | 2270(42) | 192(83) | 1.05(4) | 0.20 | (3, 7) | 0.998(12) | 38 | 8600 |
| 246 | 38 | 2242(24) | 126(56) | 1.02(2) | 1.40 | (2,18) | 0.983(5) | 58 | 8900 |
| 253 | 37 | 2174(25) | 202(56) | 1.04(2) | 0.10 | (2, 7) | 0.981(5) | 54 | 8900 |
| 260 | 36 | 2169(23) | 255(59) | 1.05(2) | 0.46 | (2, 8) | 0.983(6) | 41 | 9900 |
| 268 | 35 | 2156(29) | 341(72) | 1.09(3) | 0.46 | (2, 7) | 0.988(6) | 54 | 8400 |
| 275 | 34 | 2161(24) | 282(65) | 1.05(2) | 0.80 | (2, 8) | 0.977(5) | 40* | 8800 |
| 284 | 33 | 2123(24) | 523(66) | 1.15(3) | 0.16 | (2, 7) | 0.997(5) | 55 | 9900 |
| 312 | 30 | 2058(26) | 571(75) | 1.16(3) | 0.48 | (2, 6) | 0.988(6) | 40* | 9900 |
| 334 | 28 | 2001(33) | 832(130) | 1.27(7) | 0.99 | (2, 6) | 1.001(9) | 54 | 5000 |
| 360 | 26 | 1965(35) | 910(124) | 1.30(7) | 0.05 | (2, 7) | 1.001(9) | 50 | 5500 |
| 390 | 24 | 1991(33) | 921(115) | 1.28(6) | 0.58 | (2,10) | 0.996(8) | 40* | 7200 |

2. The spectral function

In Figs. 19 and 20, we plot the spectral functions $\rho(\omega)$ in the 0^{++} and 2^{++} glueball channels at various temperatures. In both the channels, we observe the tendency that the thermal width grows with the increasing temperature (up to the statistical errors). To be strict, each of these curves corresponds to actually a part of the spectral function $\rho(\omega)$, i.e., it is the ground-state contribution in the spectral function rather than the original spectral function itself. This can be understood in the following way. Recall that the best-fit analysis is performed in the fit-range determined from the simultaneous plateau in

the plots of the effective center $\omega_{0;\text{eff}}(t)$ and the effective width $\Gamma_{\text{eff}}(t)$. In this fit-range, $G(t)$ is expected to be less sensitive to the existence of the higher spectral components, and hence, it becomes possible to extract only the contribution from the ground-state peak. However, in order to express $G(t)$ with the spectral function $\rho(\omega)$ (cf. Eq. (50)) in the whole region of t , the higher spectral components should be necessary even after the smearing procedure is applied. Nevertheless, the goodness of the fitting in Figs. 4, 5, 11, 12, 8, 9, 13 and 14 indicates that the contributions from the higher spectral components may be actually rather small.

3. The main result of the Breit-Wigner fit

In Fig. 21, the center $\omega_0(T)$ and the thermal width $\Gamma(T)$ of the lowest-state peak of the spectral function $\rho(\omega)$ in the 0^{++} glueball channel are plotted against temperature T . Here, the triangles denote the results for the suitable smearing with $N_{\text{smr}} = 40$, and the circles denote the results with N_{smr} , which maximizes the normalized overlap $g_\Gamma(0)$. The agreement of both results indicates that the systematic error originating from the particular choice of N_{smr} is small.

We observe that the thermal width $\Gamma(T)$ grows gradually with the increasing temperature, resulting in the significant increase near the critical temperature T_c as

$$\Gamma(T \sim T_c) \sim 300 \text{ MeV}. \quad (59)$$

The center $\omega_0(T)$ is observed to decline modestly by about 100 MeV near T_c as $\omega_0(T \sim T_c) \simeq 1440$ MeV in comparison with $\omega_0(T \sim 0) \simeq 1530$ MeV.

In Fig. 22, the center $\omega_0(T)$ and the thermal width $\Gamma(T)$ of the lowest-state peak of the spectral function $\rho(\omega)$ in the 2^{++} glueball channel are plotted against temperature T . The changes are observed less significant in the 2^{++} glueball channel than in the 0^{++} glueball channel below T_c , which, however, is followed by a sudden expansion of the thermal width $\Gamma(T)$ around $T \sim T_c$. This sudden expansion of $\Gamma(T)$ may indicate the instability of the thermal 2^{++} glueball around T_c .

In Tables IV and V, we summarize the results of the Breit-Wigner fit analysis for the 0^{++} and the 2^{++} glueballs, respectively: the center $\omega_0(T)$, the thermal width $\Gamma(T)$ and the strength parameter A of the lowest-state peak, which play the role of the fit parameters, together with the correlated χ^2/N_{DF} , the fit-range (t_1, t_2) and the normalized overlap $g_\Gamma(0)$.

As a remarkable result of the Breit-Wigner analysis, we emphasize that the gradual growth of the thermal width $\Gamma(T)$ of the 0^{++} glueball begins already far below T_c in the confinement phase. This may be an attractive feature for the experimental observation of the thermal effect.

4. Comparison of the Breit-Wigner analysis with the pole-mass analysis

Finally, we consider the relation between the pole-mass analysis and the Breit-Wigner analysis. As is mentioned before, the Breit-Wigner analysis is a straightforward extension to the pole-mass analysis. In fact, they coincide in the vanishing width limit $\Gamma \rightarrow +0$. In this limit, we have the equality,

$$m_G(T) = \omega_0(T). \quad (60)$$

However, in the presence of the width Γ , the relation between $m_G(T)$ and $\omega_0(T)$ becomes nontrivial. As a

consequence, instead of Eq. (60), we are left with the inequality,

$$m_G(T) \leq \omega_0(T). \quad (61)$$

To see this, we consider the spectral representation Eq. (5), where the temporal correlator $G(t)$ is expressed as an average of the hyperbolic cosine of frequency ω with the weight as

$$\frac{\rho(\omega)}{2 \sinh(\beta\omega/2)}. \quad (62)$$

Suppose the idealized case where the spectral function $\rho(\omega)$ is completely dominated by a single peak. In this case, Eq. (62) reads

$$W(\omega) \equiv \frac{2\pi A (\delta_\Gamma(\omega - \omega_0) - \delta_\Gamma(\omega + \omega_0))}{2 \sinh(\beta\omega/2)}. \quad (63)$$

To define the pole-mass, we approximate the weight $W(\omega)$ with the δ -functions as

$$\frac{2\pi A (\delta(\omega - m_G) + \delta(\omega + m_G))}{2 \sinh(\beta m_G/2)}, \quad (64)$$

where the pole-mass m_G is determined so as to reproduce the shape of $G(t)/G(0)$ in the fit range as faithful as possible. Note that “ $\sinh(\beta\omega/2)$ ” in the denominator of Eq. (63) works as a biased factor, which enhances the smaller ω region while suppressing the larger ω region. As a consequence of this biased factor, the peak position of $W(\omega)$ is shifted from ω_0 to a smaller value, which leads to the inequality Eq. (61).

To make a rough estimate of the pole mass m_G , we consider the peak position $\omega = \omega_{\text{max}} (> 0)$ of the weight $W(\omega)$ in Eq. (63), which is defined as

$$\left. \frac{d}{d\omega} W(\omega) \right|_{\omega=\omega_{\text{max}}} = 0. \quad (65)$$

We adopt the simple identification as

$$m_G \simeq \omega_{\text{max}}. \quad (66)$$

In the confinement phase $T < T_c$, the results of the Breit-Wigner fit indicate the inequality as

$$\omega_0 \gg \Gamma, T. \quad (67)$$

In this case, Eq. (63) can be approximated as

$$W(\omega) \simeq 2\pi A e^{-\beta\omega/2} \delta_\Gamma(\omega - \omega_0) \quad (68)$$

in the region of $\omega \sim \omega_0$. Hence, Eq. (65) reduces to

$$(\omega_{\text{max}} - \omega_0) + \frac{\beta}{4} \{(\omega_{\text{max}} - \omega_0)^2 + \Gamma^2\} \simeq 0. \quad (69)$$

As a consequence of the simple identification in Eq. (66), we find the relation among $m_G(T)$, $\omega_0(T)$ and $\Gamma(T)$ as

$$m_G(T) \simeq \omega_0(T) - \left\{ 2T - \sqrt{4T^2 - \Gamma(T)^2} \right\} \leq \omega_0(T), \quad (70)$$

which seems consistent with our numerical results below T_c .

We make a comment on the experimentally observed particle mass at finite temperature in the presence of the width Γ . In the high-energy experiments, the spectral function $\rho(\omega)$ is actually observed, providing the relevant information of the mass and the width of the particle at finite temperature. In fact, the experimentally observed mass is expected to be distributed around $m = \omega_0(T)$ with the width $\Gamma(T)$. Still, the single-cosh analysis is attractive from the economical viewpoint, because the Breit-Wigner analysis is rather hard to perform. As long as the width Γ is enough narrow, the pole-mass $m_G(T)$ provides a good approximation of the peak position $\omega_0(T)$ in $\rho(\omega)$. Hence, the pole-mass $m_G(T)$ can be regarded as the thermal particle mass in this case. However, when the width Γ becomes wide, the pole-mass $m_G(T)$ obtained from the single-cosh analysis suffers from the effect of the biased factor “ $\sinh(\beta\omega/2)$ ” in the denominator in Eq. (62). Therefore, $m_G(T)$ is shifted from ω_0 to a smaller value, and the Breit-Wigner analysis is preferable. As is demonstrated before, the Breit-Wigner analysis physically means the direct measurement of the pole position of the low-lying particle in the complex ω -plane, i.e., the shape of the low-lying peak in the spectral function $\rho(\omega)$. It provides the mass and the width of the particle at finite temperature as the center $\omega_0(T)$ and the width $\Gamma(T)$, respectively.

VII. SUMMARY AND CONCLUDING REMARKS

We have studied the thermal properties of the 0^{++} and 2^{++} glueballs using SU(3) anisotropic lattice QCD with $\beta_{\text{lat}} = 6.25$, the renormalized anisotropy $\xi \equiv a_s/a_t = 4$ over the lattice of the size $20^3 \times N_t$ with $N_t = 24, 26, 28, 30, 33, 34, 35, 36, 37, 38, 40, 43, 45, 50, 72$ at the quenched level.

First, we have measured the temporal correlators $G(t)$ for the lowest 0^{++} and 2^{++} glueballs using more than 5,000 gauge configurations at each temperature. In this calculation, we have adopted the smearing method to construct the suitable operator for the lowest-lying 0^{++} and 2^{++} glueballs on the lattice. We have also provided an analytical consideration on the physical meaning of the smearing procedure based on the spatial distribution of the gluon field in the smeared operator.

Next, we have performed the pole-mass measurements of the thermal glueballs from $G(t)$ by adopting the procedure used in the standard hadron mass measurements. For the lowest 0^{++} glueball, we have observed a significant pole-mass reduction of about 300 MeV near T_c or

$m_G(T \simeq T_c) \simeq 0.8m_G(T \sim 0)$, while its size remains almost unchanged as $\rho(T) \simeq 0.4$ fm. This pole-mass shift is actually much larger than any other lattice-QCD results of pole-mass shifts which have been ever observed in the meson sector [13, 14] with the same analysis as ours.

We have made a consideration on the QCD phase transition by using a phenomenological effective model, i.e., the closed packing model. By means of the closed packing model, we have made an analytical estimate of the critical temperature T_c by using the lattice data on the pole-mass $m_G(T)$ and the size $\rho(T)$ of the thermal 0^{++} glueball as inputs. We have encountered with a puzzle of the smallness of T_c in comparison with the rather large glueball mass.

Finally, for completeness, we have performed a more general new fit-analysis of the temporal glueball correlator $G(t)$ as an attempt to take into account the effects of the possible appearance of the thermal width $\Gamma(T)$ of the bound-state peak. We have proposed the Breit-Wigner form as a generalized fit-function $g_\Gamma(t)$ for the lowest-peak in the spectral function $\rho(\omega)$ of the temporal correlator $G(t)$ at finite temperature. This ansatz is also applicable to the temporal correlators of various thermal hadrons. In this advanced analysis, we have found a significant broadening of the lowest-glueball peak as $\Gamma(T) \sim 300$ MeV near T_c as well as a rather modest reduction in its center of about 100 MeV.

We have investigated also the temporal correlators of the color-singlet modes corresponding to the glueballs in the deconfinement phase. We have found that the thermal width $\Gamma(T)$ increases monotonically with increasing temperature both in the 0^{++} and the 2^{++} glueball channels. However, from only our lattice data, it is difficult to determine whether or not such color singlet modes may really survive above T_c as meta stable modes. The detailed studies are left for the future.

In this way, both of these two analyses have indicated the significant thermal effects of the lowlying thermal 0^{++} glueball near T_c , such as the considerable pole-mass reduction or the width broadening. Therefore, the thermal properties of glueball may provide an interesting signal of the precritical phenomenon of the QGP creation in the future experiment in RHIC. For more direct comparison with the experiment, it is desirable to include the dynamical-quark effect.

Acknowledgement

We would like to thank T. Doi for his useful comments. H. S. is supported by Grant for Scientific Research (No.12640274) from Ministry of Education, Culture, Science and Technology, Japan. H. M. is supported by Japan Society for the Promotion of Science for Young Scientists. The lattice QCD Monte Carlo calculations have been performed on NEC SX-5 at Research Center for Nuclear Physics (RCNP) in Osaka University.

-
- [1] W. Greiner and A. Schäfer, “Quantum Chromodynamics”, (Springer-Verlag, Berlin, 1994) 1.
 - [2] T. Hashimoto, K. Hirose, T. Kanki and O. Miyamura, Phys. Rev. Lett. **57**, 2123 (1986).
 - [3] T. Matsui and H. Satz, Phys. Lett. **B178**, 416 (1986).
 - [4] G. Boyd, J. Engels, F. Karsch, E. Laermann, C. Legeland, M. Lutgemeier, B. Petersson, Nucl. Phys. **B469**, 419 (1996).
 - [5] F. Karsch, E. Laermann and A. Peikert, Nucl. Phys. **B605**, 579 (2001).
 - [6] T. Hatsuda and T. Kunihiro, Phys. Rev. Lett. **55**, 158 (1985); Phys. Lett. **B185**, 304 (1987).
 - [7] H. Ichie, H. Suganuma and H. Toki, Phys. Rev. **D52**, 2944 (1995).
 - [8] CERES Collaboration, Phys. Rev. Lett. **75**, 1272 (1995).
 - [9] V.L. Eletsky, B.L. Ioffe, J.I. Kapusta, Eur. Phys. J. **A3**, 381 (1998); Nucl. Phys. **A661**, 514 (1999).
 - [10] H. Matsufuru et al., Proc. of *Quantum Chromodynamics and Color Confinement*, edited by H. Suganuma et al. (World Scientific, 2001) 246.
 - [11] O. Kaczmarek, F. Karsch, E. Laermann and M. Lutgemeier, Phys. Rev. **D62**, 034021 (2000).
 - [12] C. DeTar and J.B. Kogut, Phys. Rev. Lett. **59**, 399 (1987).
 - [13] QCD-TARO Collaboration, Phys. Rev. **D63**, 054501 (2001).
 - [14] T. Umeda, R. Katayama, O. Miyamura and H. Matsufuru, Int. J. Mod. Phys. **A16**, 2215 (2001).
 - [15] N. Ishii, H. Suganuma and H. Matsufuru, Proc. of *Lepton Scattering, Hadrons and QCD*, edited by W. Melnitchouk et al. (World Scientific, 2001) 252.
 - [16] N. Ishii, H. Suganuma and H. Matsufuru, Phys. Rev. **D** in press.
 - [17] E. Laermann and P. Schmidt, Eur. Phys. J. **C20**, 541 (2001).
 - [18] B. Grossmass, S. Gupta, U. M. Heller and F. Karsch, Nucl. Phys. **B417**, 289 (1994).
 - [19] S. Datta and S. Gupta, Nucl. Phys. **B534**, 392 (1998).
 - [20] S. Datta and S. Gupta, Phys. Lett. **B471**, 382 (2000).
 - [21] T. R. Klassen, Nucl. Phys. **B533**, 557 (1998).
 - [22] C. J. Morningstar and M. Peardon, Phys. Rev. **D60**, 034509 (1999), and references therein.
 - [23] J. Sexton, A. Vaccarino and D. Weingarten, Phys. Rev. Lett. **75**, 4563 (1995), and references therein.
 - [24] M. J. Teper, OUTP-98-88-P (1998), hep-th/9812187.
 - [25] I. Montvay and G. Münster, *Quantum Fields on a Lattice*, (Cambridge, 1994) 1.
 - [26] H. J. Rothe, *Lattice Gauge Theories*, (World Scientific, 1992) 1.
 - [27] T. Hashimoto, A. Nakamura and I. O. Stamatescu, Nucl. Phys. **B400**, 267 (1993).
 - [28] APE Collaboration, Phys. Lett. **B192**, 163 (1987).
 - [29] T. T. Takahashi, H. Matsufuru, Y. Nemoto and H. Suganuma, Phys. Rev. Lett. **86**, 18 (2001).
 - [30] Y. Iwasaki, K. Kanaya, T. Kaneko and T. Yoshié, Phys. Rev. **D56**, 151 (1997).
 - [31] P. de Forcrand and K.-F. Liu, Phys. Rev. Lett. **69**, 245 (1992).
 - [32] T. Schafer and E. Shuryak, Phys. Rev. Lett. **75**, 1707 (1995).
 - [33] W.-S. Hou, C.-S. Luo, G.-G. Wong, Phys. Rev. **D64**, 014028 (2001).

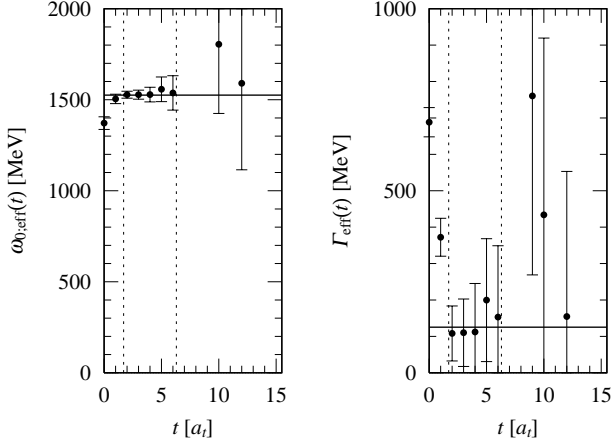
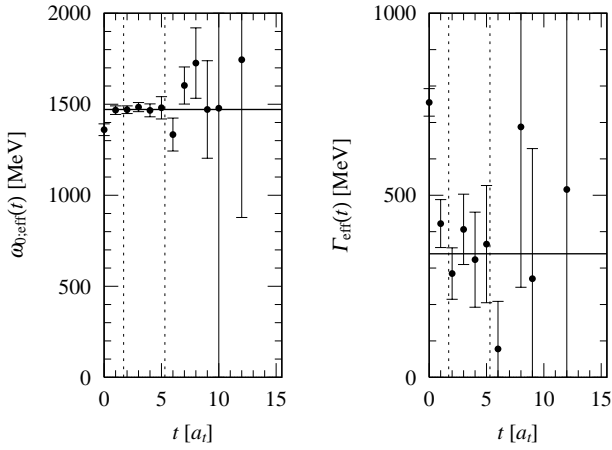
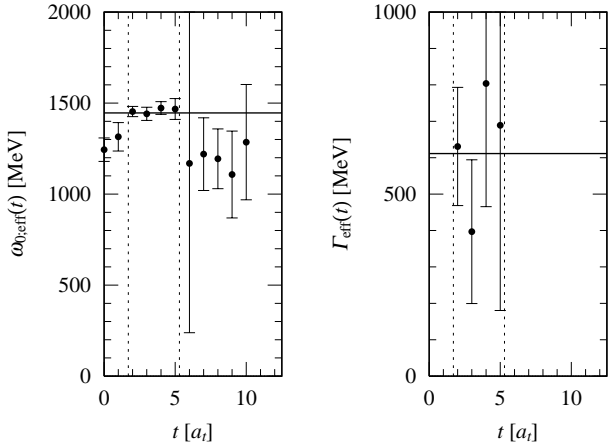
(a) $T = 130$ MeV(b) $T = 253$ MeV(c) $T = 390$ MeV

FIG. 16: The effective center $\omega_{0,\text{eff}}(t)$ and the effective width $\Gamma_{\text{eff}}(t)$ of the 0^{++} glueball correlator with the suitable smearing Eq. (32) at various temperatures (a) $T = 130$ MeV, (b) $T = 253$ MeV and (c) $T = 390$ MeV. The errorbars are estimated with the jackknife analysis. The solid lines represents the results of the best-fit analysis of Breit-Wigner type. The vertical dotted lines indicate the simultaneous plateaus, which are used to determine the fit-ranges in the Breit-Wigner fit analysis.

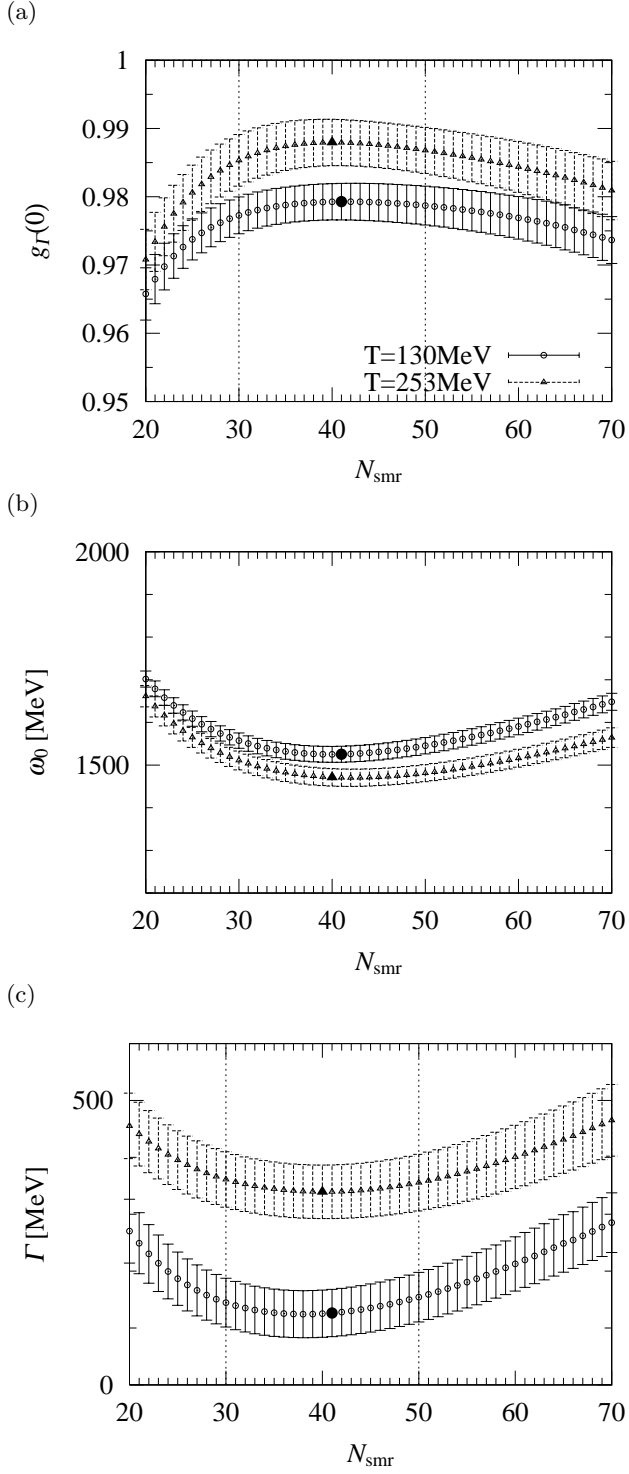


FIG. 17: The normalized overlap $g_T(0)$, the center ω_0 and the thermal width Γ of the lowest peak of the 0^{++} glueball against the smearing number N_{smr} in the confinement phase at $T = 130$ MeV and 250 MeV, which are denoted by the circle and the triangle, respectively. The solid symbols denote the data where $g_T(0)$ becomes maximum. Both for ω_0 and Γ , the N_{smr} -dependence is small in the region of $30 \leq N_{\text{smr}} \leq 50$.

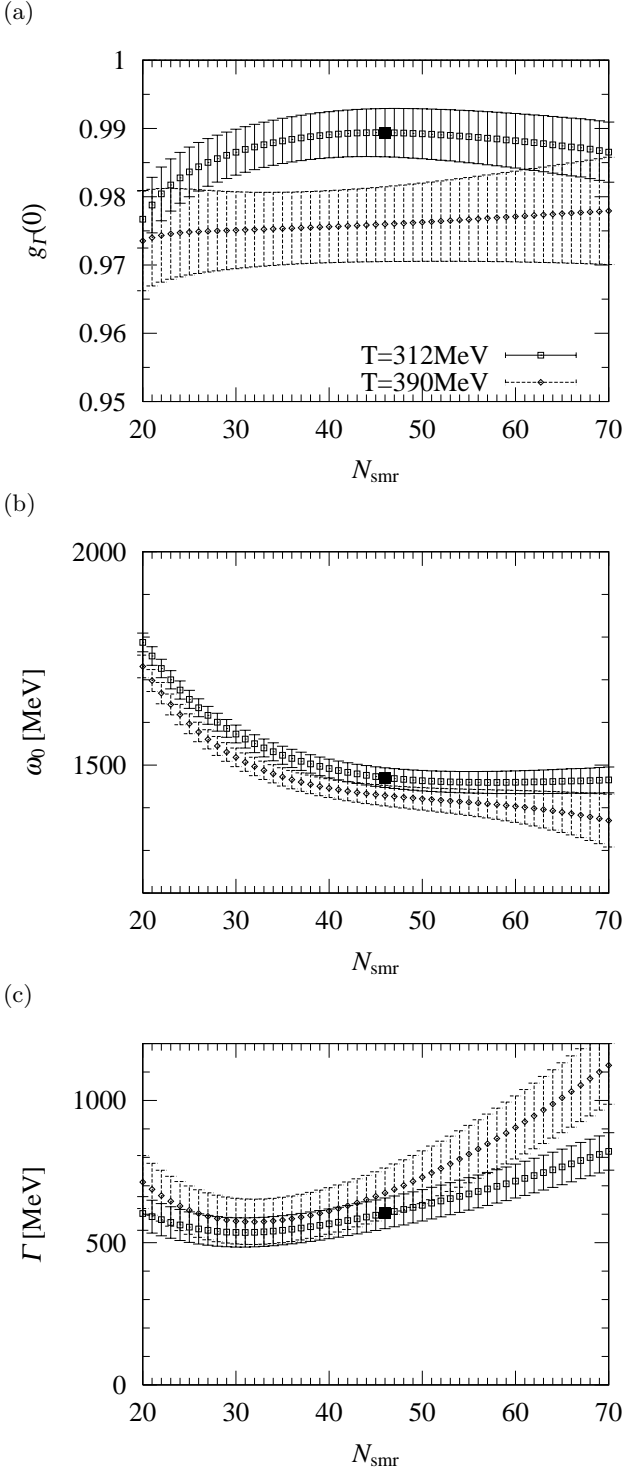


FIG. 18: The similar figure as Fig. 17 in the deconfinement phase at $T = 312$ MeV and 390 MeV, denoted by the square and diamond, respectively. The absence of the solid diamond is due to the missing maximum of the normalized overlap $g_T(0)$ in the region $N_{\text{smr}} < 70$. Above T_c , the normalized overlap $g_T(0)$ becomes less sensitive to N_{smr} , whereas the N_{smr} -dependence of the width Γ is rather large in this region.

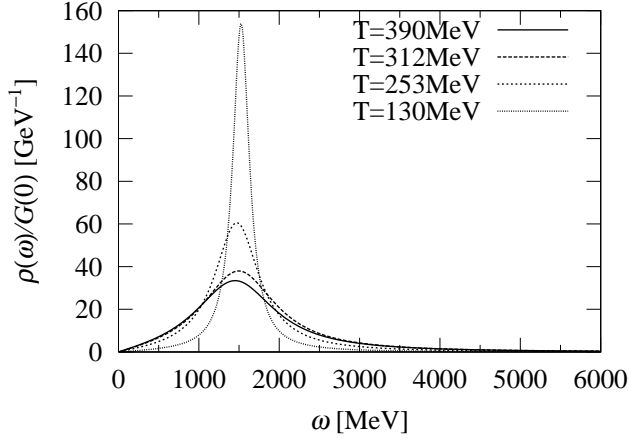


FIG. 19: The spectral function $\rho(\omega)$ of the lowest 0^{++} glueball at $T = 130, 253, 312, 390$ MeV, obtained from the Breit-Wigner fit analysis of the 0^{++} -glueball temporal correlator $G(t)/G(t)$ with the suitable smearing as Eq. (32). The shape of $\rho(\omega)$ is gradually changed with the increasing temperature even below T_c .

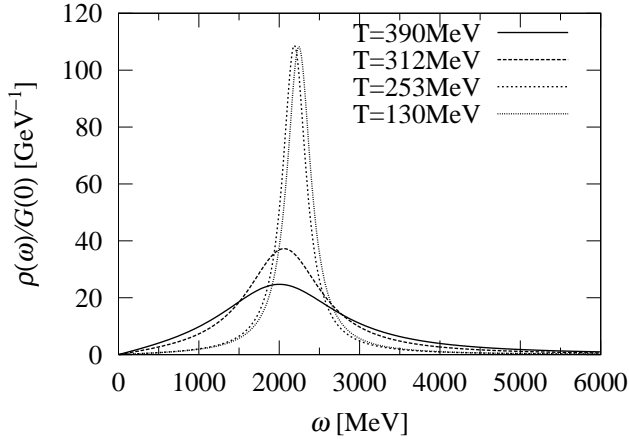
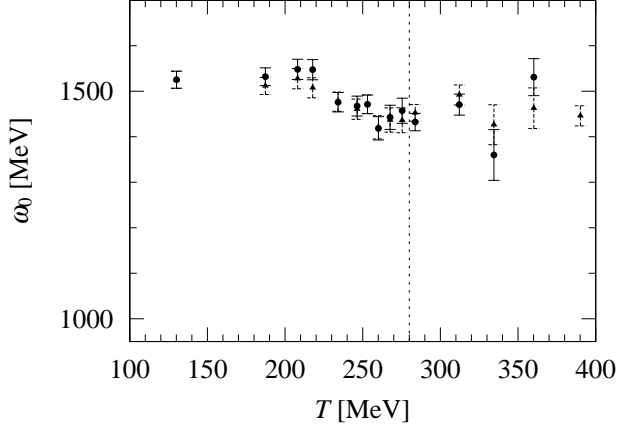


FIG. 20: The spectral function $\rho(\omega)$ of the lowest 2^{++} glueball at $T = 130, 253, 312, 390$ MeV, obtained from the Breit-Wigner fit analysis of the 2^{++} -glueball temporal correlator $G(t)/G(t)$ with the suitable smearing as Eq. (32). Whereas the shape of $\rho(\omega)$ remains almost unchanged below T_c , it begins to change significantly around T_c .

(a)



(b)

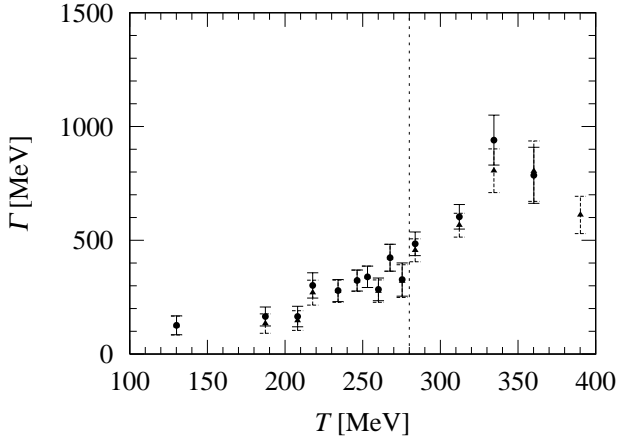
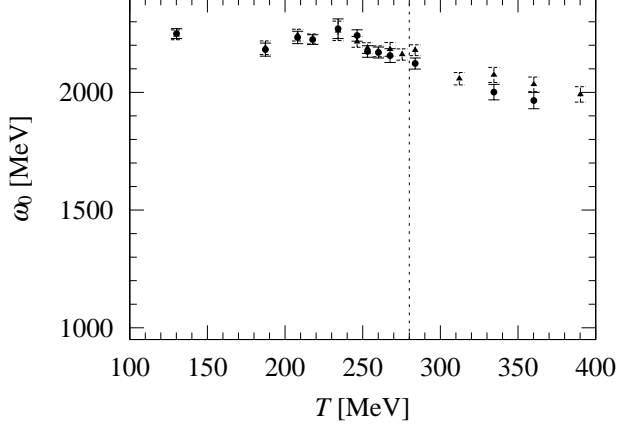


FIG. 21: (a) The center $\omega_0(T)$ and (b) the width $\Gamma(T)$ of the lowest-state peak in the spectral function $\rho(\omega)$ for the 0^{++} glueball against temperature T in the Breit-Wigner fit analysis. The triangle denotes the results associated with the suitable smearing as Eq. (32), and the circle denote the results with N_{smr} listed in Table IV, which maximizes the normalized overlap $g_\Gamma(0)$. The agreement of both results indicates that the systematic error originating from the particular choice of N_{smr} is small.

(a)



(b)

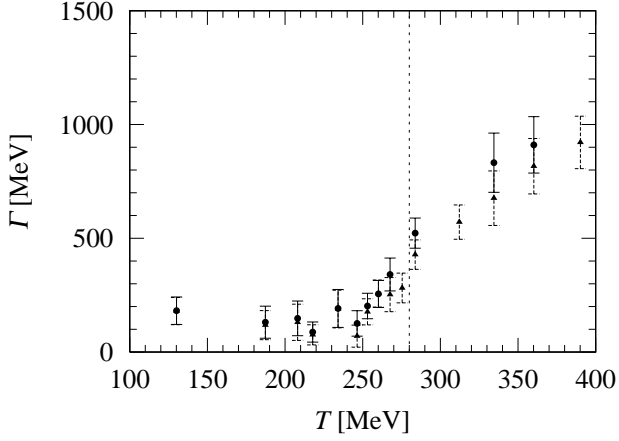


FIG. 22: (a) The center $\omega_0(T)$ and (b) the width $\Gamma(T)$ of the lowest-state peak in the spectral function $\rho(\omega)$ for the 2^{++} glueball against temperature T in the Breit-Wigner fit analysis. The triangle denotes the results in the typical suitable smearing with $N_{\text{smr}} = 40$, and the circle denote the results with N_{smr} listed in Table V, which maximizes the normalized overlap $g_\Gamma(0)$. The agreement of both results indicates the small systematic error on the choice of N_{smr} .

